M 2023

U.PORTO
FEUP FACULDADE DE ENGENHARIA
UNIVERSIDADE DO PORTO

# POLYMERIC NANOPARTICLES FOR THE DELIVERY OF NON-ALKYLATING AGENT FOR GLIOBLASTOMA THERAPY

**MARIANA TRINDADE GUEDES DOS SANTOS GOMES**
MASTER THESIS IN CHEMICAL ENGINEERING
PRESENTED TO THE FACULTY OF ENGINEERING
OF THE UNIVERSITY OF PORTO

Master in Chemical Engineering

# *Polymeric Nanoparticles for the delivery of non-alkylating agent for Glioblastoma therapy*

## Master dissertation

of

**Mariana Trindade Guedes Dos Santos Gomes**

**Developed within the course of dissertation**

held in

**LEPABE**

lepabe
Laboratory for Process Engineering, Environment, Biotechnology and Energy

Supervisor at FEUP: **Prof. Maria do Carmo Pereira**
Joint supervisor at FEUP: **Dr. Maria João Ramalho**

U.PORTO
FEUP FACULDADE DE ENGENHARIA
UNIVERSIDADE DO PORTO

DEPARTAMENTO DE
ENGENHARIA QUÍMICA

**August 2023**

# Financial Support

This work was financially supported by: LA/P/0045/2020 (ALiCE), UIDB/00511/2020 and UIDP/00511/2020 (LEPABE), funded by national funds through FCT/MCTES (PIDDAC); project EXPL/NAN-MAT/0209/, funded by FEDER funds through COMPETE2020 – Programa Operacional Competitividade e Internacionalização (POCI) and by national funds (PIDDAC) through FCT/MCTES; Project 2SMART - engineered Smart materials for Smart citizens, with reference NORTE-01-0145-FEDER-000054, supported by Norte Portugal Regional Operational Program (NORTE 2020), under the PORTUGAL 2020 Partnership Agreement, through the European Regional Development Fund (ERDF). FCT supported M.J.R. under the Scientific Employment Stimulus - Individual Call – (CEEC-IND/01741/2021). This project has received funding from the European Union's Horizon 2020 research and innovation programme under grant agreement No 958174; and from national funds through FCT (M-ERA-NET3/0001/2021).

ALiCE ASSOCIATE LABORATORY IN CHEMICAL ENGINEERING

lepabe Laboratory for Process Engineering, Environment, Biotechnology and Energy

FCT Fundação para a Ciência e a Tecnologia · REPÚBLICA PORTUGUESA · NORTE2020 · PORTUGAL 2020 · UNIÃO EUROPEIA Fundo Europeu de Desenvolvimento Regional · M-ERA.NET

# Acknowledgments

As the culmination of a remarkable journey approaches, I am compelled to express my heartfelt gratitude to those who provided unwavering support and patience, transforming this journey into one of the most significant experiences of my academic life, and guiding me towards identifying the path I wish to pursue for the rest of my life. Foremost, I would like to extend my profound appreciation to my supervisors, Prof. Dr. Maria do Carmo Pereira and Dr. Maria João Ramalho, for their invaluable scientific guidance, unwavering assistance, and knowledge-sharing. I am sincerely grateful to them. Additionally, I extend my gratitude to my fellow colleagues at LEPABE and DEQ for their collaboration and support throughout this time. Thank you all for everything.

To all my family, that was always there supporting me throughout this year, I am so thankful for having you in my life.

To my friends, thank you so much for all the support, and happiness during these 5 years.

To João, thank you for being always there, encouraging me and believing in me.

To my sister, thank you for helping me through this hard-working time leading me always to do better and for never giving up on me.

To my father, thank you for supporting me through this and for listening to me every day talking about nanoparticles, but mostly for always believing in me.

To my mother, thank you for always being my safe place, for always giving me strength throughout this time, for being my confident, but mostly for always believing in me.

Finally, from the deep of my heart, I would like to dedicate this work to my new stars, grandparent Guedes and grandparent Jorge, who guided me all the way throughout this work and gave me hope and strength to pursuit my dream. I will never forget you.

# Resumo

O glioblastoma multiforme (GBM) é uma neoplasia extremamente invasiva que afeta o cérebro e que se caracteriza como sendo um dos tumores malignos mais fatais que afetam o sistema nervoso central. O tratamento convencional para o GBM, é comumente referido como protocolo de Stupp, e consiste na combinação remoção cirúrgica seguida de ciclos de radioterapia e quimioterapia com o fármaco temozolomida (TMZ). Esta abordagem terapêutica multimodal apresenta eficácia limitada uma vez que resulta apenas num ligeiro aumento do tempo de sobrevivência do paciente, enquanto que a recorrência do tumor é frequente.

O TMZ é o principal fármaco utilizado na quimioterapia para o tratamento do GBM. No entanto, por ser um agente alquilante apresenta algumas limitações relacionadas com os mecanismos de reparação do DNA mediados pela proteína O6-metilguanina DNA metiltransferase (MGMT). Perante estas limitações, torna-se imperativo explorar alternativas terapêuticas já aprovadas pela Food and Drug Administration (FDA). A cloroquina (CHQ) foi proposta como uma potencial solução para superar essas limitações, devido às suas propriedades como agente não alquilante, que permite superar a resistência mediada pela proteína MGMT. Adicionalmente, a existência de barreiras biológicas, como a barreira hematoencefálica (BHE), reduz consideravelmente a biodisponibilidade dos fármacos no tecido tumoral.

A utilização de sistemas de entrega de fármacos baseada em nanopartículas (NPs), é uma abordagem possível que permite aprimorar a administração e o direcionamento da CHQ para as células do GBM.

O principal objetivo deste estudo foi produzir NPs de poli(ácido láctico-co-glicólico) (PLGA) para a encapsulação de CHQ, visando o seu potencial como tratamento para o GBM.

De forma a otimizar a produção das NPs contendo CHQ, foi aplicado um Desenho Composto Central. Neste sentido, definiram-se as características físico-químicas desejáveis das NPs, como o baixo índice de polidispersão, potencial zeta negativo e tamanho inferior a 200 nm, visando facilitar a sua penetração através da BHE

As NPs de PLGA carregadas com CHQ foram produzidas com êxito, uma vez que foi alcançada uma elevada eficiência de encapsulação. Além disso, as NPs foram submetidas a um processo de conjugação com transferrina, com o objetivo de aumentar a sua especificidade em resposta à presença de recetores de transferrina que apresentam um elevado nível de expressão na superfície das células tumorais e da BHE.

Por fim, a estabilidade das NPs, assim como o perfil de libertação da CHQ foram estudados. Os resultados obtidos demostraram que as NPs são estáveis em condições fisiológicas e de armazenamento por pelo menos 3 semanas, e exibem um perfil de libertação controlado, caracterizado por uma libertação gradual e prolongada do fármaco.

**Palavras-Chave:** Glioblastoma Multiforme; Entrega no Cérebro; Agentes não alquilantes; Cloroquina ; Nanoparticulas ; ácido poli(ácido láctico-co-glicólico); Nanoterapia.

# Abstract

Glioblastoma multiforme (GBM) is an extremely invasive neoplasm that affects the brain and is characterized as one of the most fatal malignancies affecting the central nervous system (CNS). The conventional treatment for GBM, commonly referred to as the Stupp protocol, consists of neurosurgical intervention followed by cycles of combined radiotherapy and chemotherapy with temozolomide (TMZ). Regrettably, this multimodal therapeutic approach exhibits limited efficacy, yielding only modest increases in patient survival time, while frequent tumor recurrence remains a prominent challenge.

The gold standard drug for GBM chemotherapy is TMZ which an alkylating agent, although it represents some limitations related to DNA repair mechanisms mediated by the protein O6-methylguanine DNA methyltransferase (MGMT). Given these constraints it becomes imperative to explore alternative therapeutic drugs that have been already approved by the Food and Drug Administration (FDA). Chloroquine (CHQ) was proposed as a potential solution to address these limitations, since it mechanism of action is independent of the MGMT protein repair mechanism, which enables to overcome the mediated resistance of MGMT protein.

Additionally, the existence of biological barriers, such as the blood-brain barrier (BBB), considerably reduces the bioavailability of drugs in the tumor tissue. A suitable approach to address this challenge is the use of nanoparticle (NPs)-based drug delivery systems (DDS), which can improve the delivery and targeting of CHQ to GBM cells.

This study aimed to produce poly(lactic-co-glycolic acid) (PLGA) NPs loaded with CHQ as a possible treatment for GBM. To optimize the CHQ encapsulation it was used a central composite design (CCD). To this end, the desirable physicochemical characteristics of the NPs were established, including a size below 200 nm, to facilitate their crossing through the BBB, a low polydispersity index, and a negative zeta potential.

The produced CHQ-loaded PLGA NPs were successfully produced with high encapsulation efficiency (EE). Additionally, the produced NPs were submitted to a conjugation process with transferrin (Tf), in order to enhance their specificity, in response to the presence of Tf receptors (TfR) that exhibit an elevated expression level on the surface of the BBB and GBM tumor cells.

Finally, the release profile of CHQ and the stability of the developed NPs was studied. The findings demonstrated that the NPs are stable in storage and physiological conditions for at least 3 weeks and exhibited a sustained and controlled release pattern, characterized by a gradual and prolonged release of CHQ.

**Keywords:** Glioblastoma Multiforme; Brain delivery; Non-alkylating drug; Chloroquine; Nanoparticles; Polylactic-co-glycolic acid; Nanotherapy.

# Declaração

Declara, sob compromisso de honra, que este trabalho é original e que todas as contribuições não originais foram devidamente referenciadas com identificação da fonte.

Mariana Trindade Guedes dos Santos Gomes

Porto, 2 de Julho de 2023

# Index

# List of Figures

# List of Tables

# Notation and Glossary

## *List of Abbreviations*

-AAc acrylic acid
-BBB Blood-Brain Barrier
-BEV bevacizumab
-CaPi Biodegradable calcium phosphate
-CHQ Chloroquine
-CCD Central Composite Design
-CE Conjugation Efficiency
-CNS Central Nervous System
-DDSs Drug Delivery Systems
-DHA Dihydroartemisinin
-DOX Doxorubicin
-DLS Dynamic Light Scattering
-DoE Design of Experiments
-EE Encapsulation Efficiency
-FDA Food and Drug Administration
-FTIR Fourier-Transformed Infrared Spectroscopy GBM Glioblastoma Multiforme
-HA Hyaluronic acid
-MGMT $O^6$-Methylguanine-DNA Methyltransferase
-MRI Magnetic resonance imaging
-M-PEG Methoxy poly (ethylene glycol)
-MSN Mesoporous Silica
-NIPAM N-Isopropylacrylamide
-PEG Polyethylene Glycol
-PDI Polydispersity Index
-PLGA Poly (lactic-co-glycolic acid)
-POM Polyoxometalates
-PVA Polyvinyl Alcohol
-PMA Poly (methacrylic acid)
-PLA Poly (l-lactic acid)
-PEI poly (ethyleneimine)
-PEG Poly (ethylene glycol)
-RA rheumatoid arthritis
-SD Standard Deviation
-SLE systemic lupus erythematosus
-TEM Transmission Electron Microscopy
-Tf Transferrin
-TMZ Temozolomide
-TPGS alpha-tocopherol polyethylene glycol 1000 succinate
-TTF tumor treatment field therapy
-PTX Paclitaxel
-PTPP Triphenylphosphonium-functionalized hyperbranched polymer
-WHO World Health Organization
-VEGF vascular endothelial growth factor
-VEGFR vascular endothelial growth factor receptor
-ZCPH IF-8/CHQ/POM/HA
-ZP Zeta potential

## Lists of symbols

- $A$: Absorbance
- $c$: Concentration (mol/m³)
- $D$: Translation diffusion coefficient (m²/s)
- $d$: Path length of the beam (m)
- $E$: Electric field (V/m)
- $\varepsilon$: Molar Absorption Coefficient (m²/mol)
- $\varepsilon_0$: Permittivity in vacuum (F/m)
- $\varepsilon_r$: Dielectric constant
- $f(Ka)$: Henry's Function
- $I$: Intensity of the light that reaches the detector (W/m²)
- $I_0$: Intensity of the incident light beam (W/m²)
- $k$: Boltzmann constant (J/K)
- $Ka$: Ratio of the particle radius and Debye length
- $RH$: Hydrodynamic radius (m)
- $T$: Absolute temperature (K)
- $v$: Velocity (m/s)
- $\eta$: Viscosity (Pa·s or N·s/m²)
- $\zeta$: Zeta Potential (V)
- $\mu_e$: Electrophoretic mobility (m²/V·s)

# 1 Introduction

## 1.1 Framing and presentation of the work

Glioblastoma multiforme (GBM) is a grade IV glioma brain cancer which is life-threatening to many individuals affected by this cancer [1]. The estimated annual incidence of GBM is approximately 3 cases per 100,000 individuals worldwide [2].

Chloroquine (CHQ) is a non-alkylating FDA-approved drug for many diseases as malaria, systemic lupus erythematosus (SLE) and rheumatoid arthritis. It recently has shown great anti-cancer properties likely to potentiate a  treatment for cancers like GBM [3]. Unlike alkylating agents, the mechanism of action of CHQ does not involve alkylation, enabling it to effectively circumvent O6-methylguanine DNA methyltransferase (MGMT) -mediated resistance. These characteristic addresses one of the main limitations encountered in the conventional treatment approach involving the use of the gold-standard drug, temozolomide (TMZ) [4].

Despite these advantages, CHQ efficiency in its native form is limited due to its non-specific toxicity and poor pharmacokinetics[5]. but the major challenge is the ability to cross the blood-brain barrier (BBB), which is responsible for the selective transport of drugs to the brain [6].

In recent years, nanostructures have attracted significant attention due to their efficacy to permeate the BBB and targeted drug delivery [7].

The purpose of this work was to synthesize CHQ-loaded PLGA NPs for GBM therapy and enhance their efficacy through experimental design. The study aimed to achieve targeted delivery of CHQ by modifying poly(lactic-co-glycolic acid) (PLGA) NPs with transferrin (Tf), employing a dual-targeting approach for BBB and GBM tumor cells. Additionally, the study aimed to evaluate the sustained drug release under physiological conditions.

## 1.2 Organization of the dissertation

The structure of this dissertation follows a sequential arrangement of topics. It begins with Chapter 1, which provides an introduction encompassing key subjects explored throughout the study. Moving on to Chapter 2, the current state-of-the-art regarding the subject is discussed, focusing on the constraints of GBM treatment and presenting a comprehensive overview of recent advances in CHQ delivery. Chapter 3, entitled “Materials and Methods”, outlines the methodologies employed in this project. Chapter 4 is dedicated to presenting the results obtained and engaging in a thorough discussion of their implications. Following, Chapter 5 summarizes the primary conclusions of this work while also deliberating on future perspectives. Finally, Chapter 6 outlines the objectives and the respective degree of accomplishment and also a personal vision about the developed work.

# 2 Context and State of the art

## 2.1 Glioblastoma Multiforme

Gliomas are the most common malignant tumors of the central nervous system (CNS) and can be classified according to histopathological categories, this is based on its presumed cell of origin [8]. Astrocytomas are formed in astrocytes, a type of star-shaped glial cell in the cerebrum. This type of glioma usually affects the brain and sometimes the spinal cord and can be classified in four grades depending on the appearance, as well as the degree of malignancy and the potential for growth and spread [9].

Glioblastoma multiforme (GBM), is known as grade 4 astrocytoma, as classified by the World Health Organization (WHO) and is the most frequent and aggressive primary brain tumor, representing approximately 57% of all gliomas and 48% of all primary malignant central CNS tumors. The term multiforme highlights the heterogeneity of this tumor in all aspects, including clinical presentation, pathology, genetic makeup, and response to various treatments [10].

According to the literature, GBM usually arises spontaneously from neoplastic glial cells but can also be found in the spinal cord, and there is some evidence of cases of familial gliomas [11]. The majority of cases of GBM are primary gliomas (about 90%), which result from the gradual development of cancer in normal glial cells. On the other hand, secondary gliomas, which stem from lower-grade tumors, make up the remaining 10% of cases and tend to grow more slowly (over 10-15 years) than primary gliomas [12]. Although there are genetic and molecular differences between the two types of GBM, these do not exhibit significant differences in appearance [13]. The epidemiology and incidence patterns of GBM have been extensively studied, and molecular profiling has revealed biologically discrete subsets and pathways of progression in diffuse glioma [14].

The incidence of GBM varies by country and region, but globally it is estimated to be around 3 cases per 100,000 individuals per year worldwide, and it is more common in males than females. GBM is also more common in older adults, with the peak incidence occurring in individuals aged 75 to 84 years but can appear at all ages [2].

The conventional diagnosis of GBM involves a combination of imaging techniques and histopathological analysis of tissue samples. Magnetic resonance imaging (MRI) is the primary imaging modality used to diagnose and monitor GBM, as it can provide detailed information on tumor location, size, and morphology [15]. Immunohistochemistry is often used to differentiate GBM from other types of brain tumors and to assess the expression of specific biomarkers [2].

### 2.1.1 Conventional treatment and its limitations

The current standard therapy for GBM is known as the Stupp protocol. This includes a combination of maximum surgical resection, radiation therapy (RT), and chemotherapy [16]. The conventional

treatment approach for GBM also involves symptomatic treatment by addressing various symptoms such as seizures, cerebral edema, infections, depression, cognitive dysfunction, fatigue, and venous thromboembolism [17].

However, this multimodal therapy is not curative. Complete removal of the tumor is often not possible due to its invasive nature [18]. Additionally, RT can also damage healthy brain tissue, leading to side effects such as headaches, nausea, and fatigue. Despite all efforts, most patients experience recurrence within 6.9 months of their initial diagnosis [19].

The gold standard drug for GBM chemotherapy is temozolomide (TMZ) and combined with RT can increase the average survival to 14.6 months versus 12.1 months, compared with RT alone [20]. TMZ is an alkylating agent approved by the Food and Drugs Administration (FDA). TMZ works by adding an alkyl group to DNA, at different positions, including N7 guanine, N3 adenine, and O6 guanine. O6-MeG, the most carcinogenic and mutagenic of all alkylated bases, interfere with normal DNA replication and transcription, damaging it, ultimately leading to cell death. Although alkylating agents are widely used in the treatment of GBM, they have some limitations that make their use less effective in treating this type of cancer [21, 22].

One of the prevalent resistance mechanisms is the one mediated by the O6-methylguanine-DNA methyltransferase (MGMT) enzyme. This protein is a DNA "suicide" repair enzyme that repairs DNA damage caused by alkylating agents, by transferring the alkyl group from the O6 position of guanine to a cysteine residue on the enzyme itself, as schematized in figure 1. This reaction restores the DNA structure and function, effectively reversing the damage caused by any alkylating agent. The transfer of alkyl groups from DNA to MGMT is a highly specific and irreversible reaction. That is, once an enzyme repairs DNA damage, it becomes inactive and must be resynthesized to repair further. This is an important mechanism for protecting cells from the cytotoxic effects of chemotherapeutic drugs. [23].

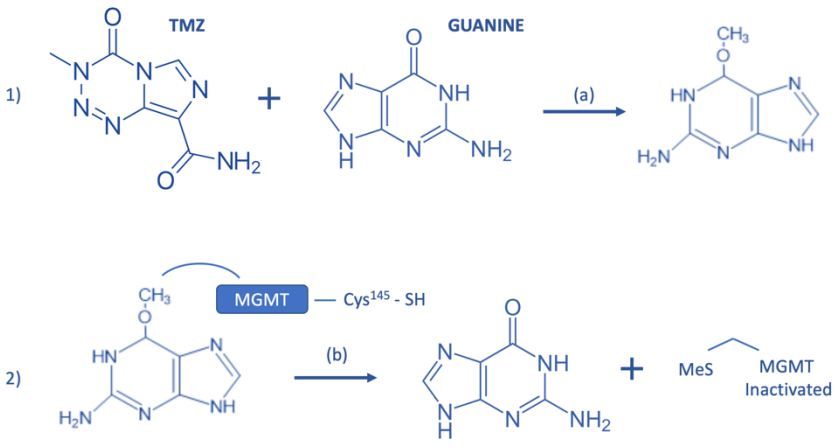


*Figure 1: 1) TMZ Mechanism, a) DNA (guanine) methylation by alkylating agents, in this case TMZ; 2) MGMT repair mechanism, b) Re- stored guanine with MeS and inactivated MGMT enzyme as reaction products.*

It is reported that between 40-60% of GBM patients exhibit high levels of production of MGMT enzyme, with unmethylated MGMT (not-silenced gene)[24].

### 2.1.2 Alternative strategies for GBM treatment

Due to the limitations of the conventional therapy, there is a need to resort to other FDA-approved therapeutic alternatives. Recent advances in the treatment of GBM promoted a wide assortment of new therapeutic approaches including combination therapy and antiangiogenic approach [25].

Combination therapies, which include a merge of various therapies such as photodynamic, magnetic hyperthermia, electrotherapy, and sonodynamic therapy, are collectively referred to as tumor treatment field therapy (TTF). One of the main advantages of TTF therapy is its minimal invasiveness, as the therapy is normally administered externally to the body. TTF therapy has shown promise in preclinical and clinical studies for a variety of cancer types, including GBM. Combining TTF therapy with other treatments, is also being investigated as a potential way to increase the effectiveness [26].

Several antiangiogenic treatments have also been developed, including monoclonal antibodies and tyrosine kinase inhibitors, to inhibit the vascular endothelial growth factor (VEGF)/vascular endothelial growth factor receptor (VEGFR) signaling pathway. Preclinical studies have shown that antiangiogenic therapy, particularly the use of the anti-VEGF monoclonal antibody, bevacizumab (BEV), inhibited tumor growth and angiogenesis in preclinical models of GBM. BEV is currently the most commonly used anti-angiogenic agent with promising results and has been approved by the FDA as a treatment for patients with GBM in combination with surgery and other anti-GBM treatments. Furthermore, a recent preclinical study reported significant inhibition of angiogenesis by berbamine, a plant-derived compound that downregulates VEGF/VEGFR [4].

Additionally, TMZ can be used combined with drugs such as BEV, irinotecan, carmustine/lomustine and carboplatin. Other drugs conjugation includes procarbazine, lomustine and vincristine cyclophosphamide and platinum-based regimens [27].

## 2.2 Non-alkylating agents as promising alternatives for GBM therapy

Despite these treatments and new research findings, GBM remains a difficult disease to treat due to its invasive nature, which makes it difficult to remove all the glioma cells, and its ability to evade the immune system. Given the current limitations and challenges in the treatment of GBM, the search for alternative therapies has become a topic of interest.

One potential avenue is repurposing drugs that have already been used to treat other diseases and that have already gone through the FDA approval, thus speeding up the process. Substances that are non-alkylating agents, i.e. paclitaxel [28] and tamoxifen [29], have particular interest, as these are known to potentially circumvent the MGMT-mediated resistance. Thus, making them more effective in the treatment of GBM than alkylating agents, because its mechanism of action will not interfere with MGMT mechanism [30].

Thus, by studying other non-alkylating drugs, researchers hope to identify new approaches to treat GBM that may be more effective and have fewer side effects. Moreover, the mechanisms of action, molecular targets, pharmacological properties, tolerability, and toxicity of approved drugs are generally well understood, allowing them to be used more effectively and safely [31].

### 2.2.1 Chloroquine for GBM therapy

Chloroquine (CHQ), 4-aminoquinoline, is an non-alkylating FDA-approved drug for many diseases as malaria, systemic lupus erythematosus (SLE) and rheumatoid arthritis (RA) [32]. Recently, CQ has shown potential in treating viral infections and cancers like GBM [3]. The chemical structure of CHQ is represented in Figure 2.

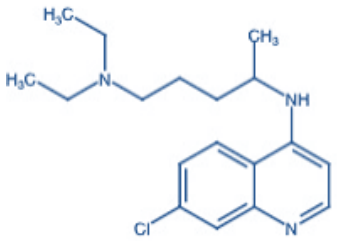


*Figure 2: Chemical Structure of CHQ (drawn in MarvinSketch).*

For cancer therapy, CHQ can be used individually or in combination with other drugs. Its use leads to an extensive enhancing of the sensitivity of tumor cells to other treatments as chemotherapy and RT. Although it can also prevent the immune escape of tumor cells, a phenomenon consisting of the growth and metastasis of tumor cells by preventing their recognition and attack by the human immune system [33, 34], it has additional advantages in regulating multiple cellular signaling pathways.

### 2.2.2 Mechanisms of Action of CHQ

Chloroquine has shown great potential for cancer treatment and several mechanisms have been identified, represented in Figure 3.

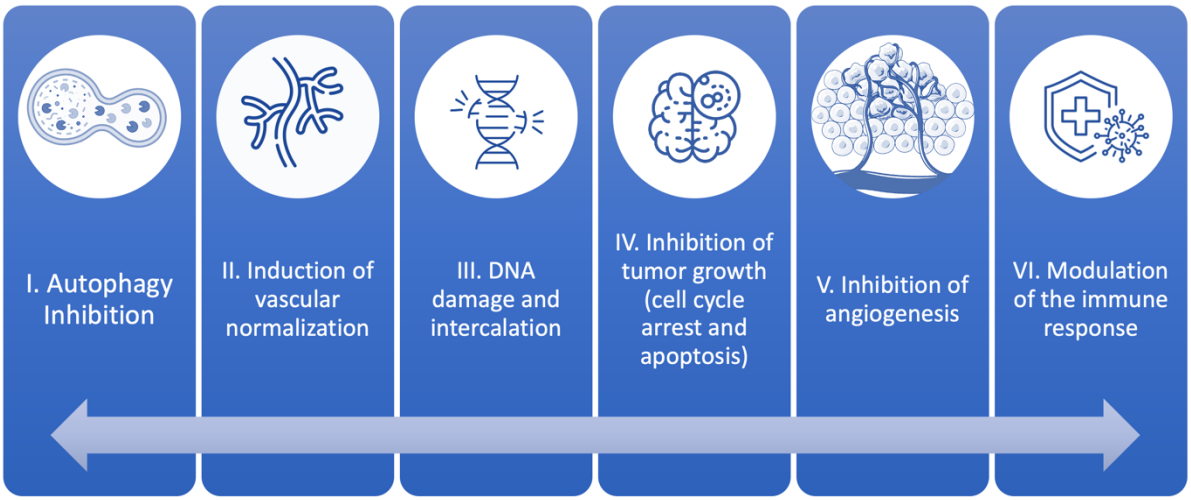


*Figure 3: CHQ mechanisms of action*

I. Thus far, the modulation of the autophagic response has been extensively studied as the primary mechanism of CHQ in both non-neoplastic and cancer cells [35].

For being a lipophilic and weakly basic tertiary amine CHQ accumulates in acidic intracellular compartments. It affects the activity of endosomes, lysosomes, autophagosomes, and autophagolysosomes by raising intra-organellar pH. CHQ has lysosomotropic properties and primarily accumulates in lysosomes, blocking the lysosome-autophagosome fusion during the late stage of autophagy. This mechanism may contribute to the cytotoxicity of chloroquine in GBM cells, and could cause the release of proteolytic enzymes, preventing the degradation of autophagic proteins, such as light chain 3B-II (LC3B-II) which damage cellular proteins, including plasma membrane-associated proteins. In this way, it prevents the generation and reusing of important supplements and metabolites, including nucleotides, amino acids, and fatty acids, causing tumor cell damage and death [36].

The optimal dose of CHQ needed to inhibit autophagy in cancer *in vivo* is not clear. Amaravadi et al.(2007), showed, in animal models, that a dose of over 50 mg/kg/day can effectively inhibit autophagy and lead to the accumulation of ineffective autophagosomes in cancer cells. However, this dose is not safe for human use [37].

II. Additionally, recent data has provided interesting evidence of other tumor–suppressing effects of CHQ independent of autophagy inhibition [38, 39].

Some studies like, Maes et al (2014) reported that CHQ has the ability to induce vascular normalization by enhancing Notch signaling in endothelial cells, which leads to improved blood perfusion in tumors and reduced metastasis, improving drug delivery and response. In this study it was not excluded the possibility that CHQ can affect vessel normalization by regulating additional molecular pathways or by affecting other stromal cells. However it was evidenced that the mechanism used by CHQ to normalize tumor vessels was autophagy-independent [40].

III. CHQ can intercalate into the DNA of tumor cells, causing DNA damage by the formation of mutations. This mechanism may contribute to the antitumor activity of chloroquine in GBM [41].

Andrew et al. (2014) reported that since CHQ is a planar molecule it has the ability to insert into DNA double helix structure, forming a stable DNA-CHQ complex. This, consequently, leads to the disruption of the DNA structure and hinders its functions, such as replication, transcription, and DNA repair. CHQ intercalation with DNA is thought to play a role in its antimalarial effects by interfering with the replication and transcription needed for the survival and spread of the malaria parasite [42].

IV. The crucial function of the tumor suppressor protein p53 is to preserve the integrity of the genome and trigger apoptosis if the damage cannot be repaired. As a result, p53 is a critical protein in safeguarding against the formation of tumors [43].

Studies conducted in both *in vitro* and *in vivo* have suggested that CHQ has the ability to stabilize the p53 protein and activate transcription of pro-apoptotic genes that are dependent on p53 [44, 45]. CHQ ability to damage DNA activating p53 signaling can lead to a transient arrest of the cell cycle, enabling DNA repair. However, if the level of DNA damage surpasses the cell's capacity for repair, this may lead to cell death [36]. Whereas the ability of CHQ to induce p53- dependent apoptosis has been well-documented [46]. Although, it has also been suggested that the activation of p53 by CHQ may be mediated by the ataxia telangiectasia mutated protein, depending on the specific cell type [47, 48].

V. In addition, inhibition of angiogenesis is gaining considerable interest as promising approach in the field of cancer therapy. Besides supplying nutrients and oxygen to tumor cells, tumor blood vessels also play a role in removing metabolic waste, leading to cancer growth and metastasis. In order to support the high proliferative rate of cancer cells, tumors need to rapidly develop a new vascular network resulting in the bad and improper formation of tumor blood vessels. This defective formation of vascular network in tumors has been associated with the involvement of some growth factors, such as angiopoietins, platelet-derived growth factor (PDGF-B), and transforming growth factor (TGF-β) [49].

Roy et al (2015), investigated *in vitro* the CHQ as a hypothesis treatment alone and in combination. This study was based in the inhibition of the enzymes responsible for TGF-β maturation in the trans-Golgi network/endosomal compartments. It was validated, using a quantitative fluorescence-based and proliferation assay, with CHQ concentration of 10 and 25 μM that has indeed the potential to block proliferation in selected GBM primary cultures as well as cell lines [50].

Another study carried out by Li et al (2016), showed that CHQ might inhibit angiogenesis via the downregulation of p-AKT, Jagged1, and Ang2, to effectively suppress cancer growth [51].

VI. Moreover, CHQ can also prevent the immune escape of tumor cells, a phenomenon consisting of the growth and metastasis of tumor cells by preventing their recognition and attack by the human immune system [33, 34].

Overall, CHQ has also a good solubility and can be rapidly absorbed through various administration routes, including oral, subcutaneous, intramuscular, and rectal.

In the following Table 1 are represented some clinical trials testing CHQ in GBMs.

*Table 1: Summary of clinical trials testing chloroquine in GBMs adapted from [36].*

| Study ID | Phase | Patient Group | | Treatment | Outcomes |
|---|---|---|---|---|---|
| | | Age | Diagnosis | | |
| **NCT00224978** | III | 18-65 | First/second recurrent or relapsed GB (WHO stage = IV) in one hemisphere | Carmustine + radiotherapy + placebo<br>vs.<br>Carmustine + radiotherapy + chloroquine | Increase medium survival from 11 to 24 months<br>No statistical significance.<br>Well tolerated[52-54]. |
| **NCT03243461** | III | 3-18 | Untreated pediatric high-grade glioma (WHO stage ≥ III) | Temozolomide + radiotherapy + valproic acid<br>vs.<br>Temozolomide + radiotherapy + chloroquine | Clinical Trial started at July 17, 2018, and the Estimated Primary Completion Date is December 31, 2023<br>No results published until now [55, 56]. |
| **NCT02432417** | II | 18-70 | Newly diagnosed IDH wild-type GB (WHO stage = IV) | Radiotherapy + chloroquine | Clinical Trial started at January 2023 and the Estimated Primary Completion Date is January 2025<br>No results published until now [57]. |

| | | | | | |
|---|---|---|---|---|---|
| **NCT02378532** | I | ≥ 18 | Newly diagnosed GB (WHO stage = IV) and confirmed MGMT and EGFRvIII status | Temozolomide + Radiotherapy + chloroquine | Study finished on July 30, 2019, with main objective to identify the maximum tolerated dose of chloroquine as a radiosensitizer. No results published until now[58]. |
| **NCT01727531** | | ≥ 18 | Solid primary tumor and at least one brain metastasis | Whole-brain radiotherapy + chloroquine | No results published until now [59]. |

### 2.2.3 Limitations of chloroquine administration

Despite the favorable evidence of anti-cancer properties of CHQ, its effectiveness as a treatment for GBM has been limited. Several adverse effects are usually reported such as ocular toxicity, associated with the disruption of the blood retinal barrier; [60] and cardiotoxicity. According to, Blignaut, M. et al (2019), low and intermediate doses administered either currently or acutely are sufficient to result in myocardial dysfunction[61]. Additionally, CHQ's interaction with other drugs, such as azithromycin, increases the risk of adverse effects, including ventricular arrhythmia[62].

Its potential to develop resistance is another limitation, as glioma cells upregulate autophagy in response to stress conditions potentially enabling tumor maintenance and metastasis despite CHQ treatment[63, 64].

In addition, and most importantly, the blood-brain barrier (BBB), which is a protective barrier that prevents harmful substances from entering the brain, also limits the effectiveness of many neurological diseases' treatments. This barrier is highly impermeable, preventing most drugs from reaching and attack the GBM cells [6]. Thus, the delivery of CHQ to GBM cells can be challenging.

CHQ also exhibits low bioavailability due to its limited solubility in water and low absorption *in vivo*, which reduces its therapeutic efficiency [65]. Additional liabilities of these drug include pharmacokinetic profiles that require extended dosing to achieve therapeutic tissue concentrations, because of their distribution throughout the body, as opposed to preferentially accumulating in tumor tissues [66, 67].

A suitable approach to address these challenges is the use of nanoparticle (NPs)-based drug delivery systems, which can improve the delivery and targeting of CHQ to GBM cells as discussed in the following sections [66].

## 2.3 Drug Delivery Strategies for cancer therapy

In recent decades, extensive research has been devoted to nanotechnology, aiming to develop innovative techniques and products that have the potential to enhance our overall well-being, and has become the basis of various industrial applications [68]. Nanomedicine takes advantage on nanomaterials characterized by unique physicochemical and biological properties at the nanoscale ($10^{-}$

$^{9}$ m) to address various healthcare challenges such as medical devices including drug delivery systems (DDS) and diagnostic biosensors [69].

The current chemotherapeutic strategies encounter challenges regarding their lack of specificity in targeting tumor cells and their potential negative impact on healthy cells, which can lead to the activation of various drug resistance mechanisms, as previously referred [70]. Therefore, there is an urgent need to explore nanotechnology-based DDS for the administration of anti-cancer therapeutic agents since it provides notable advantages by enabling in situ delivery of drugs to specific sites, being able to cross physiological barriers, such as BBB, and allowing precise control over the rate of drug release [71].

Improving NPs properties such as, their stability and time in circulation, their ability to cross physiological barriers and to gain access to the affected anatomic sites, their bioavailability at the disease site, and their safety profile should contribute to enhanced efficacy of the cancer treatment [72].

This is only possible when producing NPs with the correct characteristics such as shape and size, since those affect their biodistribution, toxicity and ability to accumulate at specific sites in the human body. Generally, NPs must have a size below 200 nm to be considered for clinical application, since it improves their ability to permeate tumor tissues and cross biological barriers such as the BBB[73, 74]. Additionally, particles with diameter >200 nm tend to activate the lymphatic system and may be removed from circulation more rapidly[75].

In addition, modifying the surface of NPs with molecules that have specific properties and affinity for the cellular receptors may enhance their ability to target and deliver drugs to tissues that may have been previously inaccessible, thus optimizing their delivery [76]. NPs can exhibit various surface charges, including positive, negative, and neutral. Cationic NPs have the ability to efficiently penetrate cells due to interactions with the negative surface charge of the cells. Moreover, high concentrations of both anionic and cationic NPs can have detrimental effects on BBB function. Some studies have reported that negatively charged NPs demonstrate superior rates of uptake into the brain compared to NPs with neutral or positive charges [77]. Some NPs commonly used for biomedical applications are represented in Figure 4.

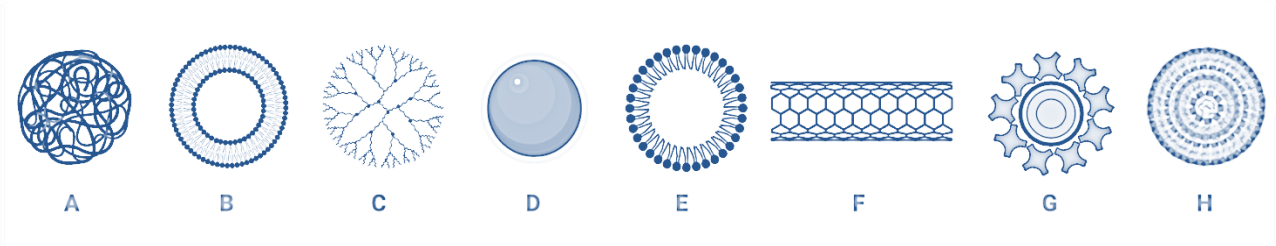


*Figure 4: Different types of nanoparticles commonly used for biomedical applications: A-Polymer; B-Liposome; C-Dendrimer; D- Gold Nanoparticle; E- Micelle; F-Carbon Nanotube; G- Quantum dot; H- Amphiphilic Cyclodextrins.*

One suitable approach to target tumor tissues leans on passive targeting, taking advantage of the enhanced permeability and retention (EPR) effect and the second approach relies on an active targeting strategy by the attachment of specific surface ligands [78].

NPs of certain sizes can effectively leverage the EPR effect, enabling them to cross the underdeveloped and permeable endothelium of tumor blood capillaries. As a result, these NPs tend to accumulate significantly more in tumor tissue compared to normal tissues. Consequently, they can persist within the tumor for extended periods, ranging from days to weeks, due to the deficient lymphatic drainage [79].

In figure 5 is represented both normal and dysfunctional lymphatic drainage system that ultimately leads to EPR effect.

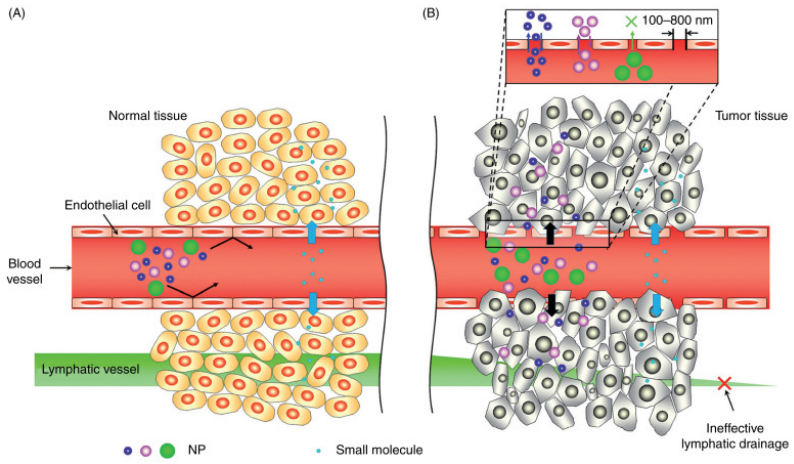


*Figure 5: Schematic showing differential uptake of NPs and small molecules based on their size across (A) normal and (B) cancerous tissues [80].*

In addition, tumor cells, due to their rapid growth, have a higher metabolic rate and increased demand for oxygen and nutrients, consequently, this metabolic demand leads to the stimulation of glycolysis, resulting in an acidic environment surrounding the tumor tissue [81]. Taking advantage of this, pH-sensitive NPs have been designed to be stable at physiological pH 7.4 but degraded to release drug molecules at the acidic pH [82].

However, the passive targeting strategy approach has limited benefits when employed for the treatment of CNS disorders, such as GBM. The main obstacle for the DDS is the BBB and the Blood-Brain Tumor Barrier (BBTB), which are the most selective barriers since it effectively prevents the unrestricted passage of blood-borne solutes into the CNS's extracellular fluid [83]. Within the brain, the vascular gaps typically range from 7 to 200 nm, indicating an extremely impermeable BBB that restricts the transportation of NPs larger than 200 nm through this barrier [84].

Another approach to address these challenges like BBB and BBTB can be employed. Active targeting strategies involve the attachment of specific chemical moieties or ligands, such as antibodies, proteins, peptides, and nucleic acids, to the surface of NPs, enabling precise delivery to tumor sites.

These ligands are selected based on the levels of specific receptors expressed by the target cells and their ability to be taken up by the target site. Importantly, the receptors or cell surface markers should be overexpressed on the target cells to facilitate the targeted localization of the NPs [85].The most prevalent targets in GBM are transferrin (Tf), folate, chlorotoxin (CTX), angiopep-2, EGFR, VEGF, αvβ3 integrins, matrix metalloproteinases (MMP) and vascular cell adhesion molecule [86].

A widely used ligand is Tf due to the overexpression of Tf receptors (TfR) on the BBB and GBM cells. Tf has been recognized as a dual-targeting agent, and its integration onto the outer surface of the nanocarrier has been demonstrated to enhance cellular uptake. Consequently, it leads to increased drug accumulation within the cytoplasm of tumor cells [87]. *in vitro* study conducted by Dixit et al , of human glioma cancer lines (LN229 and U87) overexpressing the transferrin receptor (TfR) show a significant increase in cellular uptake for targeted conjugates as compared to untargeted particles [88].

*Figure 6* illustrates the main structural and mechanism of action differences between the nanostructures for active and passive targeting.

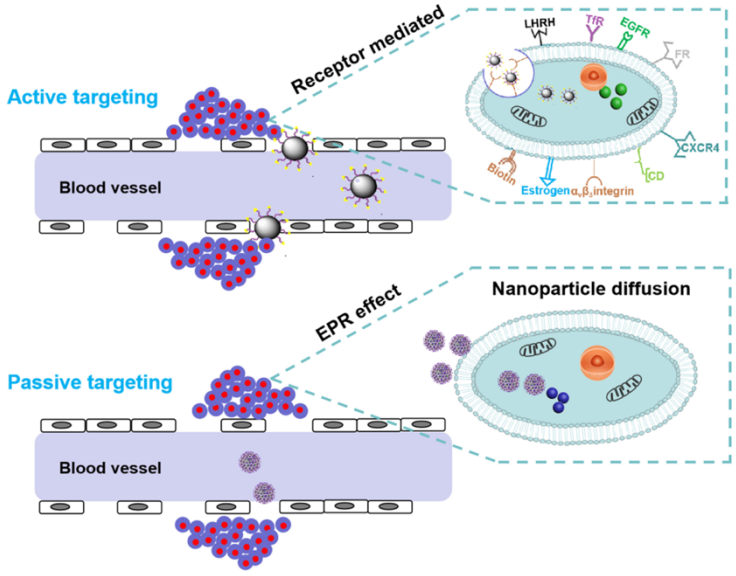


*Figure 6: Schematic representation of receptor-mediated active targeting and passive targeting through the EPR effect [85].*

## 2.4 Nanoparticles for the delivery of Chloroquine

Several nanosystems have undergone rigorous evaluation and investigation regarding their potential to integrate CHQ for the treatment of a wide range of oncologic diseases. Numerous nanocarriers with varied characteristics have been extensively explored, and the key findings from these studies are succinctly summarized below in Table A1.1 in Appendix 1.

Rashidzadeh et al. (2023) developed a poly(methacrylic acid) (PMAA) nanohydrogel for CHQ delivery [89]. The nanoformulation surface was chemically modified with methotrexate to take

advantage of its dual function, as it can act as both targeting ligand and chemotherapeutic agent. *in vitro* release experiments showed a faster release of both drugs in the presence of proteinase k enzyme and at acidic pH than at pH 7.4. This enzyme/pH-responsive behavior of the nanoformulation is explained by the break of the amide bonds between the targeting moiety and the PMAA surface at acidic environment of the tumor tissues. The anticancer potential of the nanosystem was evaluated *in vitro* using human colon cancer cells (SW480). The results showed that drug co-delivery in PMAA NPs significantly improved the efficiency of treatment by 1.3-fold when compared to combined free therapy. The NPs' biocompatibility was evaluated in human fibroblasts cells and red blood cells, and control NPs without drug revealed no cytotoxicity or hemotoxicity at concentrations up to 1.0 mg/mL. Furthermore, the nanoformulation also proved to be safe for *in vivo* oral administration with no changes in mice survival or physical activity.

Shao et al. (2018) developed PLA NPs aiming to improve the treatment of ovarian cancer by using CHQ as a chemosensitizer and co-encapsulating it with the chemotherapeutic drug DOX [65]. Aiming to prolong the circulation time of the NPs, these were coated with MPEG. The combination of CHQ and NPs increases lysosome pH, alters lysosome functions, and acts as a chemosensitizer to enhance the anticancer effects, increased drug concentration, and reduced toxicity. In addition, ovarian cancer cell lines (A2780 and SKOV3) were treated with varying doses of CHQ, and the cell viability was measured. It was observed that lower concentrations of CHQ (<20 μM) had limited inhibitory effects on cell growth in both cell lines. *in vivo* studies proved that the use of NPs for co-delivery of synergistic drugs can effectively maintain optimal synergistic proportions in both the target tissue and the target cells.

Gao et al. (2015) developed liposomes composed of cholesterol and soybean phosphatidylcholine or the co-encapsulation of PTX and CHQ, to address the PTX-resistant carcinoma [90]. The liposomal CHQ sensitized PTX by inhibiting autophagy and binding to multidrug-resistance transporters such as the P-glycoprotein (P-gp) and MDR-associated proteins (MRPs). *in vitro* studies confirmed enhanced cytotoxicity and apoptosis, improved cellular uptake, and superior tissue distribution when PTX and CHQ were co-encapsulated in liposomes compared to a mixture of PTX liposomes and CHQ liposomes individually. In vivo, the co-loaded liposome demonstrated significantly stronger anticancer effects than the PTX liposome plus CHQ liposome mixture.

Panagiotaki et al. (2017) developed a unique DDS that targets mitochondria, which shows potential for treating conditions such as cancer and neurological diseases associated with mitochondrial dysfunction [91]. The developed DDS was based on poly(ethyleneimine) (PEI) dendrimers, that were conjugated with the cation triphenylphosphonium (TPP) to specifically target the cell mitochondria. These nanocarriers form NPs with a diameter of approximately 100 nm in water. Two different formulations were prepared, one loaded with CHQ and other with DOX nanocarrier was loaded with both CHQ and DOX. This combination therapy was tested *in vitro* on DOX-resistant human prostate adenocarcinoma cell lines and demonstrated promising results. By combining the DOX-loaded and

CHQ-loaded NPs, the researchers observed enhanced cell growth inhibition even at extremely low concentrations of DOX (0.25 M). *in vivo* animal tests using immunodeficient mice implanted with DU145 human prostate cancer cells showed tumor growth inhibition throughout the three-week treatment period without any minimal side effects.

Later, the same group employed these dendrimers to the target delivery of CHQ to breast cancer cells (MCF-7, MDA-MB- 231, and SK-BR-3) [92]. For the *in vitro* studies the cells were cultured as mammospheres to mimic stem-like cells. It was observed that, contrary to free CHQ, both controls unloaded dendrimers and CHQ-loaded dendrimers inhibited the mitochondrial function leading to a reduction in cell viability, specifically in cells with a stem-like phenotype. *in vitro* studies were found to be more sensitive to PTPP-CHQ compared to PTPP alone, attributed to increased mitochondrial stress and further mitochondrial dysfunction caused by of PPTP-CHQ. The study also highlighted the role of ATM kinase in regulating the sensitivity of breast cancer cells to PTPP-CHQ treatment, particularly in breast cancer cells with a stem-like phenotype.

Yang et al. (2015) successfully developed Ca-CHQ-pDNA-PLGA-NP for gene delivery *in vivo*, for colon cancer therapy [93]. Different experimental conditions were varied such as the CA/CQ ratio, PVA amount and sonication intensity, to evaluate their effect on NPs size and DNA complex entrapment and integrity. The optimized NPs were proven to be safe both *in vitro* by showing no signs of hemolysis and toxicity in healthy cells and *in vivo* with no signs of histological damage in healthy mice. The NPs loaded with CHQ significantly enhanced gene transfection efficiency in HEK293 cells compared to CaPi-pDNA-PLGA-NPs. The increased transfection was attributed to the relatively fast release of CHQ compared to pDNA from the nanoparticles. Additionally, the NPs exhibited excellent tumor targeting efficiency, sustained circulation time, and an ideal tumor inhibition rate in a CT26 mouse model. Moreover, they demonstrated high targeting efficiency in the pancreas in a C57 AP model. Overall, the Ca-CHQ-pDNA-PLGA-NP showed promise as a targeted gene delivery candidate for both tumors and the pancreas.

Zhang et al. (2017) developed different formulations of PNIPAM nanogels labeled with a fluorescent maker (rhodamine B) [94]. The nanogels were loaded with CHQ or with DOX to treat breast cancer. The nanogels were taken up by the cells through micropinocytosis and protein-dependent endocytosis and were also found in autophagosomes, indicating a relation between autophagy and endocytosis/exocytosis. To evaluate their efficacy *in vivo*, mice with subcutaneous tumors received 7 administrations via the peritoneal cavity of 10 mg/kg of free DOX, 50 mg/kg CQ or a single dose of combined CHQ-nanogels and DOX- nanogels. The combination of both nanogels proved to be the most efficient approach to inhibit tumor growth.

Sun et al. (2019) developed pH-sensitive PLGA NPs (NPDOX+CHQ) loaded with two DOX and CHQ for anti-cancer sensitization [95]. The NPs were coated with TPGS due to its ability in enhancing cytotoxicity and inhibit drug-resistance mediated by the P-gp. NPDOX+CHQ efficiently degraded in the weakly acidic environment of tumor cell late endosomes, enabling the release of the loaded drugs.

Release experiments in acidic buffer suggested that the acidic environment of the early endosomes could triggered the release of the drugs from the NPs. CHQ inhibited cell autophagy, thus protecting DOX from degradation through autophagy. Additionally, CHQ also prevented late endosomes from fusing with lysosomes. By loading drugs into NPs, their excretion mediated by efflux pumps was reduced, and their transport across early and late endosomes leaded to facilitated pharmacological effects of CHQ and enhanced the effectiveness of DOX in the death of lung cancer cells (A549) and PTX-resistant A549 tumor cells. The dual drug-loaded NPs demonstrated a more effective inhibition of autophagy, with the inclusion of CHQ mitigating its negative effects, when compared with single-loaded NPs administered simultaneously. Overall, NPDOX+CHQ enhanced the anti-cancer actions of DOX, increased drug concentration in the nucleus and reversed multidrug resistance.

Zhao et al. (2015) developed chitosan NPs for the co-encapsulation of gefitinib and CHQ, for the treatment of liver carcinoma [96]. The chitosan NPs exhibited a slow and controlled release profile, with a small particle size of approximately 81 nm and a positive zeta potential. Cell uptake studies revealed that NPs are efficiently taken up by caveolae-mediated endocytosis and micropinocytosis in a time-dependent manner. The co-delivery of gefitinib and CHQ using chitosan NPs improved cell proliferation inhibition rates and enhanced cell apoptosis compared to the administration of free gefitinib or gefitinib-loaded NPs alone, by inhibiting autophagy that is associated with the development of drug resistance.

Peng et al. (2021) developed NPs for the co-encapsulation of CHQ and other antimalarial drug - DHA – that has shown promising anti-cancer effects, particularly when used in combination therapy [97]. However, the distinct pharmacokinetics properties of DHA and CHQ limited their synergistic effect in cancer treatment, leading to varied *in vivo* outcomes. To overcome this limitation, the group developed liposomes capable of simultaneously delivering DHA and CHQ to prevent the growth and metastasis of colorectal cancer. The prepared RLNP/DC formulation demonstrated favorable cytotoxicity and effectively suppressed invasion and metastasis in human colorectal cancer (HCT116) cells when tested *in vitro*. To assess the therapeutic potential *in vivo*, a mouse model of orthotopic colorectal cancer metastasis was established. The RLNP/DC formulation proved to enhance the anti-proliferative and anti-metastatic effects, confirming its efficacy against colorectal cancer.

Wang et al. (2022) developed a zeolitic imidazolate metal organic framework (ZIF-8) nanoplatform containing polyoxometalates for ovarian cancer photothermal therapy [98]. To address phototherapy-associated inflammation that may promote tumor regeneration and resistance, the nanoformulation was co-loaded with CHQ. Additionally, the nanoformulation was coated with HA via electrostatic interactions due to its tumor targeting ability and high biocompatibility. The ZIF-8/CHQ/POM nanoplatform exhibited remarkable anti-inflammatory properties, due to its ability to scavenge ROS at the cellular level. The ZCPH exhibited precise targeting to specific marker CD44 on the tumor cell and satisfied dose-dependent toxicity toward SKOV3 cells.

Joshi et al. (2012) developed gold NPs, with a size around 7 nm, that were modified by 11-mercaptoundecanoic acid that provided thiol groups for the conjugation with CHQ to investigate their potential use as breast cancer diagnosis and treatment[99]. The drug release kinetics of GNP-CHQ NPs showed that CHQ was released at an acidic pH. In human breast cancer cells (MCF-7), the anticancer efficacy of GNP-CHQ was proven. The viability of the treated MCF-7 cells was determined after exposure to various concentrations of GNP-CHQ conjugates. Necrosis mediated by CHQ-induced autophagy was found to be the primary mechanism of cell death as demonstrated by flow cytometry analysis.

Matsumoto et al. (2021) aimed to lower CHQ dosages and create a practical pre-treatment that specifically targets Pancreatic stellate cells (PSC) [100]. It was developed PLGA NPs that were loaded with CHQ. *In vivo* model of mice bearing orthotopic pancreatic tumors was used to evaluate the biodistribution of the developed PLGA nanosystem. The results revealed that it successfully delivered the drug to pancreatic tumors, while increasing blood circulation time and delaying liver metabolism. To assess the efficacy of free CHQ and loaded CHQ as their ability in enhancing the efficacy of other anticancer drug, animals were treated with different drug combination and dosages of of free gemcitabine, NPs-CHQ, and/or CHQ. At lower CQH dosages, NPs-CHQ decreased the density of activated PSCs and greatly slowed tumor growth when combined with gemcitabine. NPs-CHQ efficiently reduced PSC activation and may be a promising novel pre-treatment strategy for pancreatic ductal adenocarcinoma.

Bhattarai et al. (2010) prepared mesoporous silica NPs for the co-delivery of CHQ with DNA or siRNA plasmids. for melanoma therapy [101]. The NPs were coated with MPEG and polycations (PDMAEMA and PDEAEMA) to allow for nucleic acids conjugation. - NPs loaded with CHQ significantly increased the transfection activity of both types of nucleic acids under investigation, demonstrating the potential of the particles for drug/gene and drug/siRNA combination delivery. To further evaluate the effectiveness of mesoporus silica NPs in drug delivery, complete research of the *in vivo* stability of the NPs, as well as assessment of the influence of drug loading is needed.

# 3 Materials and Methods

## 3.1 Materials

Polyvinyl alcohol 4-88 (Mowiol ® 4-88, MW 31,000) (PVA), PLGA Resomer® RG 503 H (50:50; MW 24,000 – 38,000, cardodiimide (EDC) (MW 191.70), holo-Transferrin human (MW 80.00, purity ≥ 98%) and Chloroquine diphosphate salt (MW 515.86), were acquired from Sigma Aldrich (St. Louis, MO, USA). Ethyl acetate (99.6%, ACS reagent, MW 88.11) (EA) was purchased from BioVision (Waltham, MA, EUA). Thermo ScientificTM PierceTM BCA Protein Assay Kit was purchased from Fisher Scientific (Hampton, NH, USA) .

## 3.2 Preparation of CHQ loaded PLGA NPs

PLGA NPs can be prepared by a single-emulsion or double emulsion-evaporation method depending on the hydrophobicity of the drug in use. Since CHQ is very soluble in water, double emulsion-evaporation method was employed for the preparation of CHQ loaded PLGA NPs. This approach involves conducting emulsification through a two-step process.

As preliminary experiments, five different NPs formulations were prepared by varying some experimental variables as shown in table 2.

*Table 2: Preliminary experiments varying some experimental variables.*

| Batch ID | PLGA mass (mg) | Sonication amplitude (%) | Sonication cycles (n) | Organic solvent/water ratio (µL) |
|---|---|---|---|---|
| **T0** | 10 | 70% | 1+1 | **1000/500** |
| **T1** | 20 | 70% | 1+1 | **1000/500** |
| **T2** | 10 | 70% | 2+2 | **1000/500** |
| **T3** | 10 | 40% | 1+1 | **1000/500** |
| **T4** | 10 | 100% | 1+1 | **1000/500** |
| **T5** | 10 | 70% | 1+1 | **1000/750** |

For NPs preparation, firstly, the organic phase solution was prepared with a known amount of PLGA in ethyl acetate (EA). Secondly, a water-in-oil emulsion was prepared by adding a drop-by-drop solution of 1.0 mg of CHQ in ultrapure water, and subsequently was subjected to mechanical agitation using a vortex (Heidolph Reax Top Vortex Mixer, Heidolph instruments GmbH & Co., Schwabach, Germany).

To obtain nanosized droplets, and, consequently, NPs with pretended sizes, the emulsion was subjected to sonication (UP400S ultrasonic processor, Hielscher, Berlin, Germany). Different number of cycles and amplitudes of sonication were tested as described in table 2.

To the pre-prepared emulsion was added drop-by-drop another aqueous phase, with 1% polyvinyl alcohol (PVA). Following that, the obtained water-oil-water emulsion underwent mechanical agitation and sonication steps, as aforementioned. The samples were submitted to a continuous stirring (Colosquid, ika®, magnetic stirrer) until the organic solvent is completely evaporated. Then, the suspension of NPs was stored at a temperature of 4°C, since at low temperature NPs tend to maintain the integrity of the encapsulated drug and, also, inhibits particle aggregation. The preparation steps are illustrated in the following Figure 7.

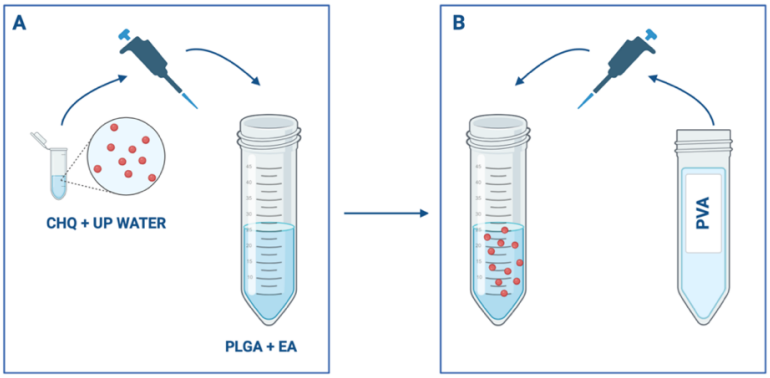


*Figure 7: A. Water-in-oil Emulsion; B. Water-in-oil-in-water Emulsion*

Finally, the NPs were collected by centrifugation (MiniSpin®plus, Eppendorf, Germany) in a progressive manner, with increasing speeds and durations for each successive run and then, resuspended in ultrapure water. Centrifugation is employed to separate the NPs from the remaining components by exploiting the differences of density. The supernatant was saved for further analysis.

## 3.3 Experimental Design and Protocol Optimization

To optimize the preparation protocol of NPs, a design of experiments (DoE) was implemented in this study. DoE offers a fast and rigorous approach to understand the impact of input factors on output responses in pharmaceutical products. This method is more efficient than the traditional one factor at a time (OFAT) technique, which is costly and time-consuming. By systematically and simultaneously varying experimental parameters (independent variables) is possible to obtain full knowledge of its relationship with the studied responses (dependent variables) in a reduced number of experiments, resulting in improved data quality. Overall, the use of DoE enables a faster and more accurate optimization of the NPs preparation protocol, enhancing the efficiency of the process [102].

The choice of experimental design in use depends on the specific objectives and variables under investigation. In this study, a Central Composite Design (CCD) was implemented using the Design Expert Software (13.0.5.0 version, Stat-Ease Inc., Minneapolis, USA). CCD is the most commonly used approach since it allows the exploration of both linear and nonlinear relationships between variables in

fewer required experiments, and also enables the assessment of quadratic effects [103]. The CCD incorporates a fractional factorial design with center points (0) and axial points (α) to estimate the model's curvature. The chosen experimental variables, represented in table 3, that were the quantity of PLGA, amplitude of sonication, percentage of PVA and organic solvent/water ratio. The variables were varied and studied at five levels (-α, -1, 0, +1, +α) to develop a formulation with optimal characteristics such as size, polydispersity index (PDI), zeta potential, encapsulation efficiency (EE) and process yield. α value (1.41421) was proposed by the design expert software automatically when choosing the practical model (K>5). The choice of the experimental variables and applied levels was based on the results of the preliminary experiments described in the previous section.

*Table 3: Parameters of the Experimental Design*

| Parameter | Units | Applied Level | | | | | Responses | Units |
|---|---|---|---|---|---|---|---|---|
| | | **-α** | **- 1** | **0** | **+ 1** | **+ α** | **Size** | nm |
| **$m_{PLGA}$** | mg | 1.645 | 12.0 | 37.0 | 62.0 | 72.355 | **PDI** | - |
| **%PVA** | % (w/v) | 0.172 | 1.0 | 3.0 | 5.0 | 5.828 | **Zeta potential** | mV |
| **$V_{WATER}$** | mL | 0.0154 | 0.15 | 0.475 | 0.8 | 0.9346 | **EE** | % |
| **% Sonication** | unit | 29.645 | 40.0 | 65.0 | 90.0 | 100.355 | **Yield** | % |

**Note:** $m_{PLGA}$ - PLGA mass; $\%_{PVA}$ – percentage of PVA; $V_{water}$ – volume of ultrapure water; % Sonication – amplitude of sonication; PDI- polydispersity index; EE- encapsulation efficiency.

Based on the model, the software suggested the preparation of 27 independent formulations, with 3 of them representing center points to assess experimental reproducibility and fit the regression model. Table 4 provides a summary of the experimental design and the corresponding obtained responses.

*Table 4: Overview and outcomes of the experimental plan.*

| Run Order | Independent Variables | | | | Dependent Variables | | | | |
|---|---|---|---|---|---|---|---|---|---|
| | $m_{PLGA}$ | $\%_{PVA}$ | $V_{WATER}$ | Sonication cycles | Size (nm) | PDI | Zeta Potential (mV) | EE (%) | Yield (%) |
| **1** | -1 | -1 | -1 | -1 | 182 | 0.08 | -13.8 | 18.1 | 93.2 |
| **2** | +1 | -1 | -1 | -1 | 209 | 0.07 | -10.3 | 37.1 | 87.8 |
| **3** | -1 | +1 | -1 | -1 | 164 | 0.12 | -17.6 | 77.4 | 79.5 |
| **4** | +1 | +1 | -1 | -1 | 205 | 0.07 | -11.1 | 16.5 | 90.0 |
| **5** | -1 | -1 | +1 | -1 | 145 | 0.16 | -20.8 | 62.6 | 75.2 |
| **6** | +1 | -1 | +1 | -1 | 167 | 0.09 | -11.8 | 32.5 | 97.7 |
| **7** | -1 | +1 | +1 | -1 | 138 | 0.15 | -13.0 | 1.3 | 86.2 |

| | | | | | | | | | |
|---|---|---|---|---|---|---|---|---|---|
| **8** | +1 | +1 | +1 | -1 | 156 | 0.04 | -13.7 | 3.5 | 75.6 |
| **9** | -1 | -1 | -1 | +1 | 175 | 0.10 | -13.8 | 25.9 | 91.4 |
| **10** | +1 | -1 | -1 | +1 | 207 | 0.07 | -12.6 | 7.8 | 92.8 |
| **11** | -1 | +1 | -1 | +1 | 154 | 0.08 | -14.2 | 7.7 | 98.1 |
| **12** | +1 | +1 | -1 | +1 | 201 | 0.07 | -12.0 | 30.4 | 84.4 |
| **13** | -1 | -1 | +1 | +1 | 145 | 0.06 | -18.3 | 6.4 | 85.4 |
| **14** | +1 | -1 | +1 | +1 | 183 | 0.06 | -13.2 | 25.1 | 82.9 |
| **15** | -1 | +1 | +1 | +1 | 142 | 0.05 | -20.7 | 81.1 | 69.1 |
| **16** | +1 | +1 | +1 | +1 | 181 | 0.05 | -11.6 | 38.4 | 91.3 |
| **17** | -α | 0 | 0 | 0 | 130 | 0.12 | -21.7 | 18.5 | 79.3 |
| **18** | +α | 0 | 0 | 0 | 181 | 0.07 | -10.1 | 9.7 | 76.6 |
| **19** | 0 | -α | 0 | 0 | 172 | 0.07 | -13.6 | 8.0 | 92.8 |
| **20** | 0 | +α | 0 | 0 | 154 | 0.05 | -9.39 | 15.0 | 85.6 |
| **21** | 0 | 0 | -α | 0 | 467 | 0.40 | -13.3 | 5.9 | 72.9 |
| **22** | 0 | 0 | +α | 0 | 158 | 0.04 | -13.2 | 2.3 | 85.5 |
| **23** | 0 | 0 | 0 | -α | 163 | 0.10 | -15.5 | 13.4 | 81.3 |
| **24** | 0 | 0 | 0 | +α | 184 | 0.08 | -11.2 | 18.7 | 91.2 |
| **25** | 0 | 0 | 0 | 0 | 176 | 0.06 | -11.7 | 24.8 | 97.9 |
| **26** | 0 | 0 | 0 | 0 | 185 | 0.06 | -11.4 | 23.5 | 94.8 |
| **27** | 0 | 0 | 0 | 0 | 187 | 0.05 | -12.5 | 24.8 | 93.6 |

A mathematical regression model was fitted individually to each response variable, establishing a correlation between the experimental parameters and the investigated responses.

$$Y = b_0 + b_1X_1 + \cdots + b_kX_k + b_{12}X_1X_2 + b_{13}X_1X_3 + \cdots + b_{k-1,k}X_{k-1}X_k + b_{11}X_1{}^2 + \cdots + b_{kk}X_k{}^2 + \epsilon \quad (1)$$

In this equation, the dependent variables (response variables) are denoted by Y, the independent variables are denoted by $Xk$, the overall mean response (intercept constant) is represented by $b0$, and the regression coefficients (RC) are represented by $bk$. $K$ represents the number of independent variables, and $\epsilon$ represents the error term.

ANOVA was then conducted for the statistical analysis to determine the optimal experimental conditions for producing NPs suitable for drug delivery to the brain (size below 200 nm, low PDI values,

negative zeta potential). P-values below 0.05, at a 95% confidence level, were considered significant, indicating statistically significant effects or interactions.

## 3.4 NPs Physicochemical Characterization

The NPs underwent physicochemical characterization, which involved measuring their size (nm), polydispersity index (PDI), and zeta potential (mV). Dynamic Light Scattering combined with Laser Doppler Electrophoresis was employed for this purpose. The measurements were conducted using a ZetaSizer Nano ZS instrument from Malvern Instruments, UK, and the data obtained were analyzed using the ZetaSizer software (version 8, Malvern).

### 3.4.1 Dynamic Light Scattering

Dynamic Light Scattering (DLS) is a technique used to analyze the size distribution of particles or molecules in suspension. It provides information about the hydrodynamic radius of particles, which is related to their size and shape. DLS is based on the Brownian motion principle, where particles in a suspension scatter light, causing fluctuations in the scattered intensity. By analyzing these intensity fluctuations over time using a correlation function, which provides information about the speed at which the particles move, DLS can determine the diffusion coefficient of particles (*D*), which is directly related to their size and shape [104].

Considering a constant temperature and a known dispersant viscosity, it is possible to calculate the hydrodynamic radius of the particles (*Rh*) from the diffusion coefficient, using the Stokes-Einstein equation:

$$Rh = \frac{kT}{6\pi\eta D} \tag{2}$$

Where *T* is the absolute temperature, $\eta$ the solvent viscosity of the medium, *k* is the Boltzmann constant, and *D* is the diffusion coefficient.

The NP format was assumed to be a hypothetical sphere for the measurements. Consequently, the equipment measured the hydrodynamic radius of the NP, considering this assumption along with the NP's solvation shell. As a result, the displayed output value slightly exceeds the actual radius of the NP [105].

In the context of DLS, the PDI can also be calculated as the ratio of the square of the standard deviation to the mean of the particle diameter. It provides an indication of how narrow or broad the distribution of particle sizes is within a sample. A PDI value of 0 indicates a monodisperse sample, where all particles have the same size. On the other hand, a PDI value closer to 1 indicates a highly polydisperse sample, with a wide range of particle sizes [106].

For the measurement of the hydrodynamic diameter and, a standard cell (Sarstedt®) made of polystyrene was used and a dilution in ultrapure water (1:10) was performed for a final concentration of NPs of 1.2 mg/mL. The refractive index of water as the dispersant at 25ºC was set to 1.330, while the viscosity was set to 0.8872 cP. The polymer refractive index was fixed at 1.590, and the absorption was set at 0.010.

### 3.4.2 Laser Doppler Velocimetry

DLS can be combined with Laser Doppler Velocimetry, to obtain the zeta potential ($\zeta$) of the NPs. Zeta Potential (ZP) is a key parameter that characterizes the surface charge and the electric potential at the interface of the NPs in a suspension. The electric potential of a surface refers to the energy needed to transport a unit positive charge from an infinite distance to the surface in question, without experiencing any acceleration.

The magnitude and sign of the zeta potential are indicative of the degree of repulsion or attraction between particles in suspension. A higher magnitude of zeta potential suggests stronger electrostatic repulsion, resulting in greater stability and resistance to particle aggregation or flocculation. On the other hand, a low ZP value indicates weaker repulsion, making the particles more prone to aggregation. When a charged particle is suspended in a liquid, a double layer is formed consisting of the Stern layer and the Diffuse layer. The Stern layer comprises ions of opposite charge to the particle, while the Diffuse layer consists of more freely moving ions. The boundary of this double layer is marked by the slipping plane [107], as represented in figure 8.

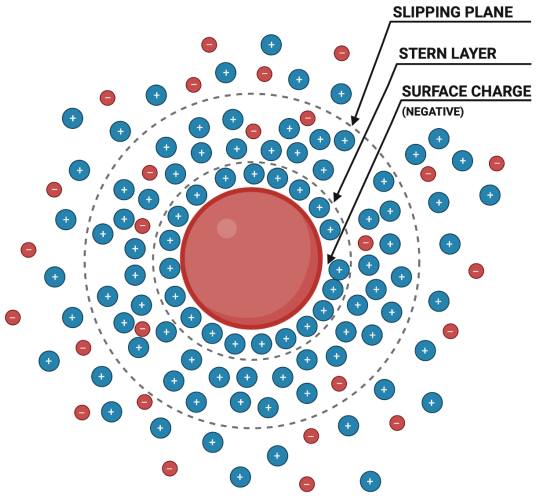


*Figure 8:Representation of the different layers involved in zeta potential measurement.*

Since ZP cannot be measured directly, it is measured using different techniques such as Laser Doppler Velocimetry. This consists in the subjection of the sample to an electric field, allowing the determination of the electrophoretic mobility (μe) of the particles. The equation below allows for the

calculation of this property using the known values for the particle velocity ($v$) and the induced electric field ($E$):

$$\mu_e = \frac{v}{E} \tag{3}$$

Once determined the electrophoresis mobility, the zeta potential can be calculated by the Helm-holz-Smoluchowshi equation:

$$\mu_e = \frac{\varepsilon\zeta}{4\pi\eta} \tag{4}$$

Where $\xi$ is the zeta potential; ε is the dielectric constant of vacuum; and $\eta$ is the viscosity coefficient of the dispersant [108].

To analyze the zeta potential of the nanoparticles (NPs), a DST1070 cell from Malvern Panalytical was employed. The cell consisted of two gold-plated beryllium electrodes, which facilitated the generation of the necessary electric field for zeta potential determination. To achieve a final NP concentration of 1.2 mg/mL, a dilution in ultrapure water at a ratio of 1:10 was used. The ZetaSizer software performed three measurements for each sample using the Smoluchowski model. The measurements incorporated the dielectric constant and viscosity values of water, set at 78.5 and 0.8872 cP, respectively.

## 3.5 Determination of the Encapsulation Efficiency

Encapsulation Efficiency (EE) refers to the proportion of drug encapsulated within the NPs compared to the total amount of drug added, and it is usually expressed in percentage. High EE indicates a more efficient and successful encapsulation process, ensuring a higher concentration of the desired substance is retained within the carrier system. The EE of the CHQ-loaded NPs was determined with an indirect method by quantifying the non-encapsulated drug present in the supernatant, obtained after centrifugation as described in the section 3.2., by UV-Vis spectrophotometry. This non-invasive method allows the measurement of light absorption in relation to different wavelengths.

To obtain the concentration of the non-encapsulated drug in relation with the absorbance measured, the Lambert-Beer law was used. The Lambert-Beer law is known as a fundamental principle in spectroscopy that describes the relationship between the concentration of a solute in a solution and the amount of light absorbed by that solution and is represented below[109]:

$$A = \varepsilon c d = -\log\left(\frac{I}{I_0}\right) \tag{5}$$

Where, $A$ represents the absorbance, $\varepsilon$ the molar absorption coefficient, $c$ the concentration; $d$ the path length of the measuring beam in the sample, $I$ the light that reached the detector, $I_0$ is the incident light beam.

Free CHQ was quantified by the UV-vis absorbance spectra at a $\lambda_{max} = 342$ nm using a microplate reader (Synergy 2 Microplate Reader, BioTek, UK). The obtained absorbance values were correlated to a CHQ calibration curve in PVA (figure A2.1, Appendix A2).

The EE (%) values for CHQ were determined using the following equation:

$$EE\ (\%) = \frac{total\ amount\ of\ CHQ - amount\ of\ free\ CHQ}{total\ amount\ of\ CHQ}\ x\ 100 \qquad (6)$$

## 3.6 Preparation of the Transferrin Functionalized NPs

The conjugation of transferrin (Tf) with NPs provides a targeted and efficient delivery system. This conjugation enables the Tf-functionalized NPs to selectively recognize and bind to cells with elevated Tf receptor (TfR) levels, such as GBM cells [110]. The targeted delivery approach offers advantages including specific accumulation at the desired site, reduced off-target effects, and minimized systemic toxicity [111].

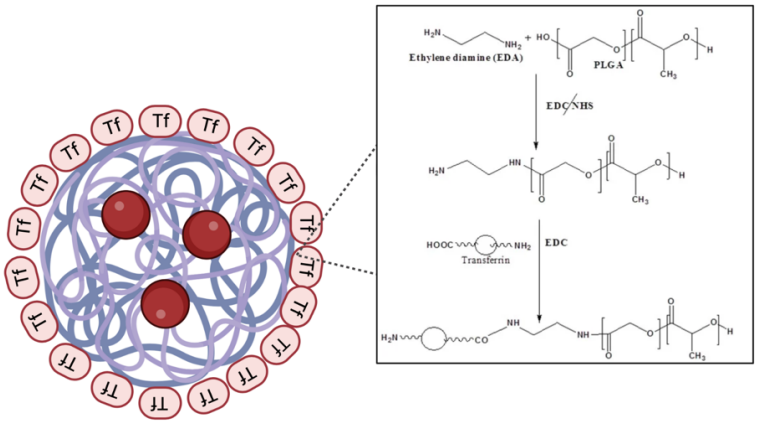


*Figure 9:CHQ loaded PLGA NPs conjugated with Tf and respective mechanism from [112].*

The CHQ-NPs were conjugated with Tf by a carbodiimide coupling reaction. PLGA carboxylic groups werea ctivated by a N-(3-Dimethylaminopropyl)-N'-ethylcarbodiimide hydrochloride (EDC) aqueous solution that was added to the NPs suspension at a 20x molar excess and maintained at continuously agitation for 30 minutes at room temperature. Subsequently, excess of Tf was added to the NPs in the form of an aqueous solution, with the aim of achieving an approximate ratio of 100 Tf molecules per NP. The sample was subjected to continuous agitation at room temperature for a duration of 1 hour. Following the incubation period, the excess of EDC and unbound Tf were removed from the Tf-conjugated PLGA NPs by sequential centrifugation steps. The resulting Tf-modified CHQ-loaded PLGA NPs were then resuspended in ultra-pure water. The non-bounded Tf present in the supernatant was quantified using a bicinchoninic acid (BCA) protein assay to assess the efficiency of the conjugation process as described in the next section.

## 3.7 Determination of Tf Conjugation Efficiency

With the aim of determining the Tf conjugation efficiency (CE) to CHQ-NPs, it was used the BCA Protein Assay Kit (Pierce, Bonn, Germany), which is also an indirect determination technique. This calorimetric method allows for protein quantification, and it is based on a reduction reaction of $Cu^{2+}$ to $Cu^{+}$, caused by the protein in an alkylating medium. Then, a purple-colored product is formed due to the reaction between two BCA molecules and $Cu^{+}$. This water-soluble complex exhibits a strong absorbance at $\lambda = 562$ nm that is proportional with increasing protein concentrations enabling protein quantification [113]. In this method is also used a UV-Vis spectrophotometry as described in section 3.6.

Then using a microplate reader (Synergy 2 Microplate Reader, BioTek, UK) was mixed 25 µL of each sample supernatant with 200 µL of working reagent (WR) at a ratio of 1:8 (v/v), in each well, and incubated for 30 minutes at 37ºC, with constant agitation. The WR enables the coloration reaction, and it is composed of 50 parts of bicinchoninic acid and 1 part of copper (II) sulfate pentahydrate.

Finally, with the respective calibration curve of Tf with BCA kit (appendix A2.2.) was possible to calculate the concentration of free-Tf with the respective absorbance value. The CE was determined through the following equation:

$$CE\ (\%) = \frac{\text{total amount of Tf} - \text{amount of free Tf}}{\text{total amount of Tf}}\ x\ 100 \qquad (7)$$

## 3.8 Fourier-Transformed Infrared Spectroscopy

Fourier-transformed infrared spectroscopy (FTIR) is a method employed to obtain an infrared absorption or emission spectrum from a solid, liquid, or gas. Since this technique enables the analysis of chemical compounds by detecting molecular conformations, such as functional groups, bond types and molecular interactions present in the sample [114], it was used to confirm the Tf conjugation with CHQ-NPs. The main goal of this technique is to measure how much light a sample absorbs, and converts into molecular vibration, at different wavelengths, allowing a quantitative and qualitative analysis. Since each molecule has its specific bonds, produces different vibration intensities, and, consequently, there is only one possible spectrum for each molecule. This enables an objective assessment of the samples which makes FTIR an important instrument for chemical identification. The resulting spectrum is given by absorbance/transmittance vs 1/wavelength, represented also as wavenumber ($cm^{-1}$) [115]. This technique has several advantages since it presents a non-destructive nature and simple sample preparation and acquisition, as it is a reagent free analytical tool, and also has a wide range of biomedical applications [116].

A Bruker Alpha-P FT-IR Spectrometer (Bruker Optics Inc., Billerica, MA, USA) and Opus Software (version 6.5, Bruker Optik GmbH) were used to record the FTIR spectra of the produced CHQ-PLGA NPs, Tf-CHQ PLGA NPs and for a Tf solution. For each sample, a 10 µL drop containing the NPs was directly placed into the ATR crystal, and then dried with a nitrogen flow. The spectra were captured in absorbance mode with 64 scans for each sample and background observations, and a wavenumber range of 4000-375 $cm^{-1}$. The spectra analysis was performed in GraphPad Prism (version 9.1.2, GraphPad Software, USA).

## 3.9 Transmission Electron Microscopy

To obtain a more complete characterization of the produced NPs, an electron microscope that can operate by transmitting the beam directly through the sample via transmission electron microscopy (TEM) was used. TEM is an exceeding powerful imaging method that produces high-resolution images of nano scaled samples using an electron beam enabling the visualization of the precise shape, structure, and composition of the material [117]. By modulating the electron beam and employing various detectors, multiple types of information, such as bright-field imaging, dark-field imaging, high-resolution imaging, diffraction patterns, and elemental mapping, may be obtained [118].

The sample should be prepared as a very thin foil to allow the electron to penetrate through it. Ultimately, a visual representation is created by combining the scattered electrons [119]. Several staining methods and solutions, carried out using heavy metal salts, have been developed with the aim of improving the contrast between the sample and the grids. Uranyl acetate (UA), which has been the recommended approach for morphology research on biological materials, has proven to produce the best staining results besides being low cost material [120].

In this work, for the visualization of the NPs by TEM technique, 5 µL of the prepared NPs was placed on a copper grid (Formvar/Carbon - 400 mesh Copper, Agar Scientific, UK) for 5 minutes and then stained with 2% (v/v) uranyl for 45 seconds. Ultimately, the NPs were visualized at Jeol JEM 1400 electron microscope (Japan).

## 3.10 *in vitro* release of CHQ from PLGA NPs

*in vitro* studies were done to study the release of CHQ from the produced non-conjugated and Tf-conjugated PLGA NPs. Aiming to simulate the physiological conditions, the NPs were maintained at 37°C with constant stirring in phosphate-buffered saline (PBS) (0.01 M, pH 7.4). PBS is an isotonic buffer that can simulate physiological conditions such as pH, osmolarity, and ionic concentrations [121].

To perform the experiments, the NPs were resuspended in 3 mL of PBS and separated into 10 aliquots. Then, the amount of drug released from the aliquots was measured over time at predetermined time-points. This involved centrifuging the aliquot at each time point to separate the NPs from the

supernatant at 14,500 rpm for 15 min. Through the supernatant's UV-Vis absorbance, the quantity of released CHQ was calculated. A calibration curve of CHQ in PBS (7.4 pH) was plotted to establish a correlation between the observed absorbance and the quantity of drug released (Figure A2.3 from Appendix). The following equation provides the proportion of CHQ released as a function of time:

$$CHQ_{Release}\ (\%) = \frac{\text{amount of CHQ released at time t}}{\text{amount of encapsulated CHQ}} \times 100 \quad (8)$$

## 3.11 Determination of NPs Stability

The stability of the non-modified and Tf-modified CHQ loaded PLGA NPs in different conditions was studied by DLS measurements, in terms of variations of the hydrodynamic size (nm), PDI and zeta potential (mV).

### 3.11.1 NPs Stability in storage conditions

Aiming to evaluate two different storage conditions, the NPs were kept in ultrapure water at 4ºC or room temperature, over a maximum of three weeks.

### 3.11.2 NPs Stability in simulated physiological conditions

To simulate the stability in physiological conditions, the prepared NPs were suspended in PBS (0.01 M, pH 7.4) and stored at 37ºC. These measurements were performed for a maximum of 29 days.

## 3.12 Statistical Analysis

The statistical analysis was performed using the T-Student test with a 95% confidence interval. A p-value of less than 0.05 was considered statistically significant. This test was used for the stability measurements of the prepared NPs and for comparison of the properties of non-modified and Tf-modified NPs.

# 4 Results and Discussion

## 4.1 Preliminary experiments and choice of experimental variables

Preliminary studies were conducted for the selection of the variables and their corresponding levels for the DOE implementation, by choosing the ones revealing to have the most impact on the NPs characteristics. The obtained results are presented in table 5.

*Table 5: Physicochemical characterization and EE of the NPs prepared in the preliminary studies (n=1).*

| Batch ID | Mean size (nm) | PDI | Zeta potential (mV) | EE (%) |
|---|---|---|---|---|
| **T0** | 168 | 0.06 | -13.5 | 39.1 |
| **T1** | 152 | 0.06 | -12.1 | 50.9 |
| **T2** | 167 | 0.05 | -13.7 | 46.9 |
| **T3** | 162 | 0.06 | -13.6 | 29.9 |
| **T4** | 155 | 0.05 | -12.8 | 41.2 |
| **T5** | 159 | 0.04 | -14.4 | 36.1 |

According to the experimental data summarized in table 5, the EE tends to rise with the increase of PLGA mass, amplitude and number of sonication cycles. Additionally, it also appears that the size of the PLGA NPs is affected by the amplitude of sonication. Notably, it was found that increasing the water amount in the organic solvent/water ratio increased the NP´s size.

To obtain NPs with desirable properties and EE, and based on these results, the quantity of PLGA, amplitude of sonication, percentage of PVA and volume of water were the variables chosen to be varied in the experimental design, to develop an optimal production protocol.

## 4.2 Experimental Design and Protocol Optimization

To diminish the number of experiments to optimize the protocol for CHQ encapsulation, a CCD was used with the support of the Design Expert program, which proposed a total of 27 formulations. The studied responses were the size, PDI, ZP, EE and Yield.

ANOVA was employed for the statistical analysis, and it revealed that the regression model was significant for all studied responses ($p<0.05$), except for the yield ($p>0.05$). For this reason, the yield was excluded from the model. The statistical analysis's outcomes are represented in Table A3.1 in Appendix 3 and further in Tables A3.2 to A3.6 in Appendix 3. The variable's size, PDI, ZP, and EE were fitted to a quartic regression model by the determination of regression coefficients (RCs). These coefficients describe the effect of changing variables on the responses. A positive RC

indicates a positive effect, indicating an increase in the response, while a negative RC implies the opposite effect, where an increase in the variable leads to a decrease in the response. By employing only the significant terms ($p<0.05$), the response equations for size, PDI, ZP, and EE were derived using the RCs. Detailed equations for these variables can be found in Appendix 3, corresponding to numbers A3.7, A3.8, A3.9, A3.10 respectively.

The correlation between the experimentally determined values and the predicted values for each significant variable is shown in Figure A3.1. It represents a strong agreement between the predicted values and the experimental values. The close correspondence between predicted and experimental values across these variables is reflected in the high $R^2$ values presented in Table A3.1.

### 4.2.1 Effect on NP´s Size

The NPs' size is considered a primary factor in determining the biodistribution, retention within target tissues, and cellular uptake [122]. The size is also closely linked to the NPs' ability to cross biological barriers [123]. As previously referred, smaller NPs have been found to be more effective in BBB penetration, and therefore more likely to accumulate in the brain. Therefore, optimizing the size of nanocarriers is crucial for targeted and efficient drug delivery for GBM therapy [124]. A NPs size smaller than 200 nm is considered the ideal size to be able cross the BBB [74].

The nanoformulations prepared by DoE exhibited sizes ranging between 130 nm (formulation 17) and 467 nm (formulation 21). The surface and contour plots in Figure 10 illustrate how the independent factors affected the size of the NPs.

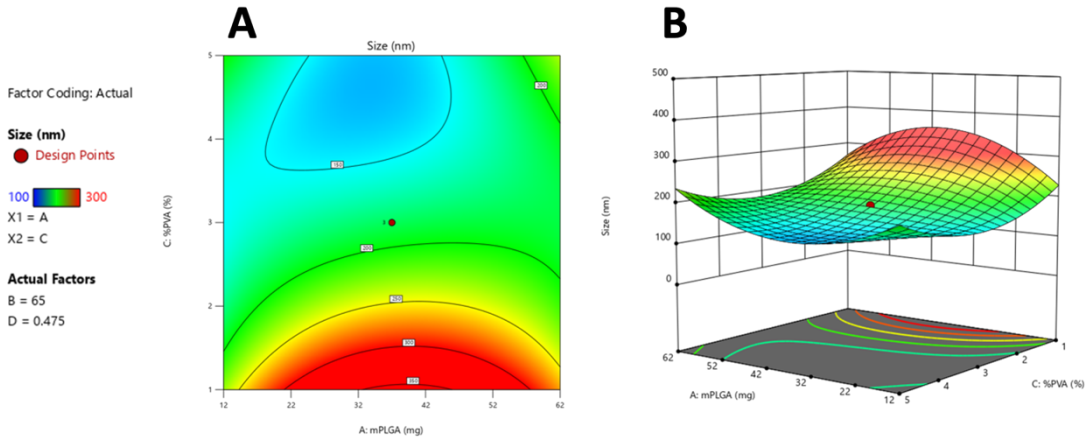


*Figure 10: (A) 2D contour plot and (B) 3D response surface plot, respectively, illustrating the effect of PLGA mass and percentage PVA on NP size. The blue tone denotes lower NP sizes, whereas the red color represents higher NP sizes.*

Considering the p-values obtained (table A3.2 in Appendix 3), it was possible to verify that the only independent variables that significantly affected the NPs' size were the % PVA and the amount of PLGA. Looking at the obtained regression equation (equation A3.7, in Appendix 3), it is possible to verify that PLGA mass has a positive effect on the NP´s size. Consequently, a higher mass of

PLGA leads to the formation of NPs with increased sizes. With higher concentration of PLGA, the viscosity of the organic phase hinders the emulsion from breaking into extremely small nano-droplets. Consequently, a substantial amount of PLGA polymer remains within the droplets, leading to the formation of NPs with a larger size [125].

In contrast, the % PVA (X2) exhibited a negative impact on the size of NPs, indicating that an increase in surfactant concentration resulted in the formation of smaller NPs. The presence of PVA contributes to the steric stabilization of the emulsion, thereby reducing the interfacial tension between the PLGA-containing oil droplets and the surrounding aqueous phase [126].

### 4.2.2 Effect on NP´s PDI

PDI is used as a measure to assess the degree of uniformity in a particle suspension, whereby higher PDI values are indicative of a larger size distribution within the particle sample. When the PDI value is less than 0.1, the sample is deemed to be monodisperse [127]. The obtained PDI values of the produced nanoformulations ranged from 0.04 (nanoformulation 8) to 0.40 (nanoformulation 21). Figure 11 illustrate the 2D contour plots and 3D response surface plots used to visually represent the effects of different independent variables on the PDI of the NPs.

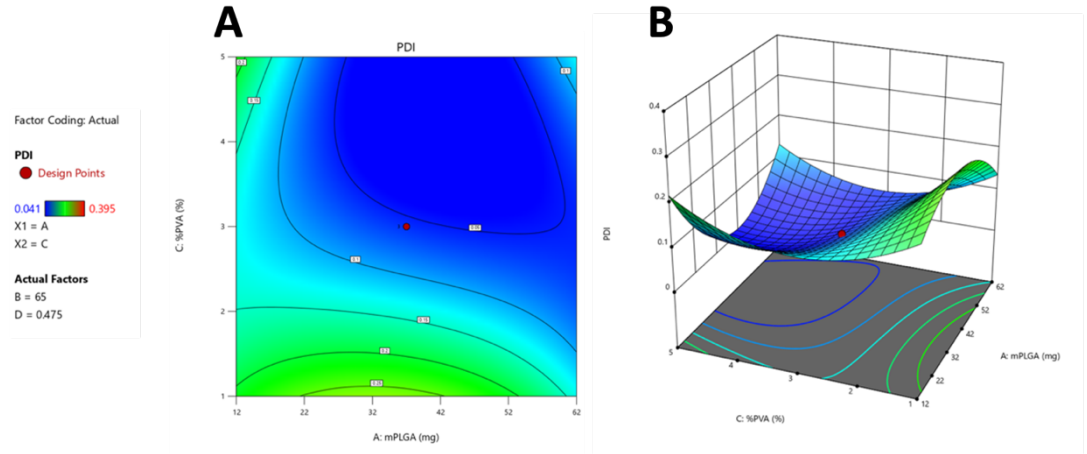


*Figure 11: (A) 2D contour plot and (B) 3D response surface plot, respectively, illustrating the effect of PLGA mass and percentage PVA on NP´s PDI. The tone of blue denotes lower PDI values, whereas the green color represents higher PDI values.*

Similarly, to the previous analysis conducted for NP´s size, the PDI was studied using the obtained equation (A3.8 in Appendix A3). In this case, also only the PLGA mass and %PVA proved to significantly affect ($p<0.05$) the response, exhibiting a negative impact on the NP´s PDI. This means that with the increase of PLGA mass and %PVA, is evident a decrease on the PDI value of the samples. Thus, changing the amount of PVA can affect how stable the colloidal system is. A higher PVA content contributes to more stability, which makes the sample more homogeneous and lowers the PDI value. PDI is influenced by the concentration of PLGA, higher polymer concentrations facilitate the creation of nanoparticle samples with significantly improved homogeneity[128]. Increasing the PLGA concentration in solution the formation time of

nanoparticles could decrease due to a higher degree of saturation of the solution. This means that the nuclei require less time to grow and reach a thermodynamic equilibrium state and the PDI tends to decrease [129].

### 4.2.3 Effect on NP´s zeta potential

The zeta potential serves as an indicator of the colloidal system's stability. Throughout the experimental design, the nanoformulations consistently exhibited negative zeta potential values due to the presence of carboxyl groups in PLGA, resulting in a range of values between -21.7 mV (nanoformulation 17) and -9.39 mV (nanoformulation 1). Additionally, the NPs' stability can be deduced from their surface characteristics. A higher absolute value of the zeta potential indicates enhanced *in vitro* stability of the NPs. This can be explained by the presence of a stronger repulsive forces, which prevents the particles approximation and, as a result, prevents the formation of aggregates [130]. The 2D contour and 3D response surface plots that provided an outline of the impact of the various independent variables on the NP´s ZP are shown in figures 12 and 13, respectively.

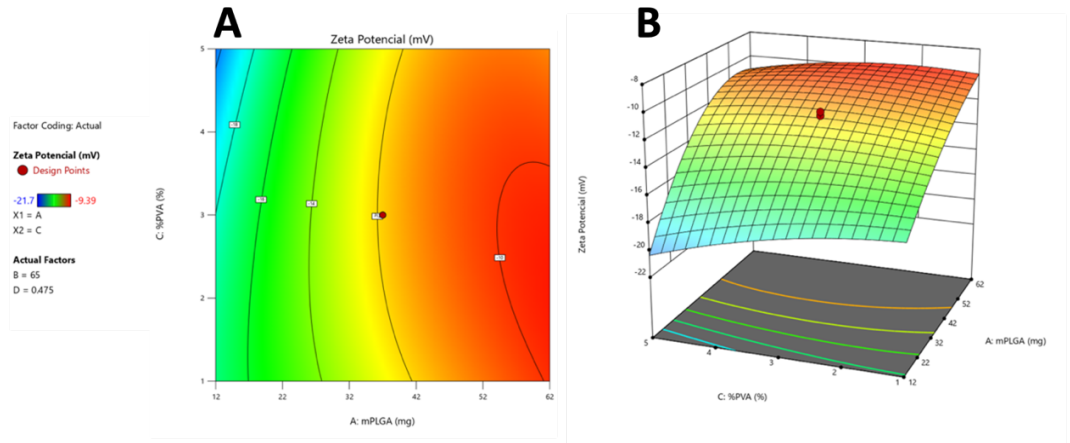


*Figure 12: (A) 2D contour plot and (B) 3D response surface plot, respectively, illustrating the effect of PLGA mass and % of PVA on NP´s ZP. The tone of blue denotes lower ZP values, whereas the red color represents higher ZP values.*

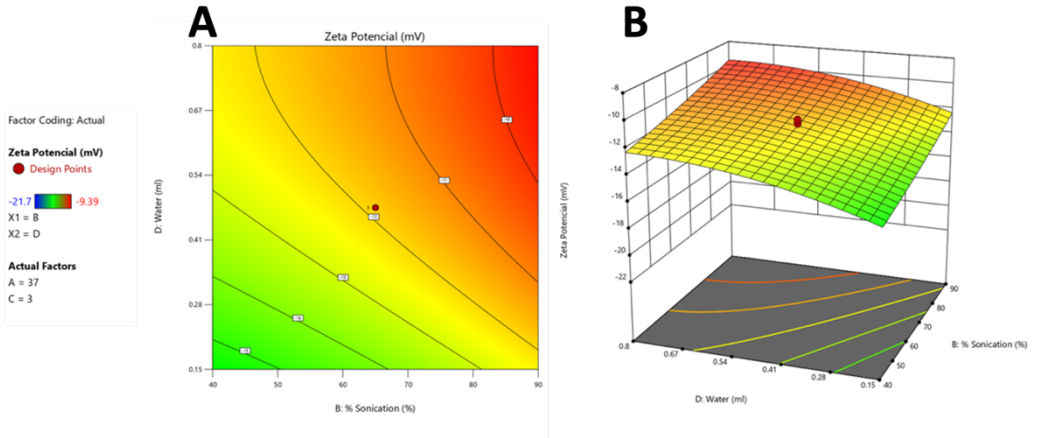


*Figure 13:(A) 2D contour plot and (B) 3D response surface plot, respectively, illustrating the effect of % of sonication and water volume on NP´s ZP. The green tone denotes lower ZP values, whereas the red color represents higher ZP values.*

Trough the analysis of the respective regression equation (equation A3.9, Appendix 3), it is possible to conclude that PLGA mass, % of sonication and water volume have a positive effect on the ZP of the NPs. This represents an increase of the NP´s ZP with an increase of the independent parameters. By increasing the amplitude of sonication, it is estimated that the formed NPs are smaller. Also, smaller NPs have higher surface area and, consequently absorb more PVA on the surface and increase the surface charge [131]. An increase on the PLGA mass also leads to an increase of the zeta potential.

### 4.2.4 Effect on NP´s EE

The EE of the produced NPs ranged from 1.4% (formulation 7) to 81.1% (formulation 15). Figures 14 and 15 show graphic representations of the impact of several independent variables on the EE of the NPs in the form of 2D contour plots and 3D response surface plots.

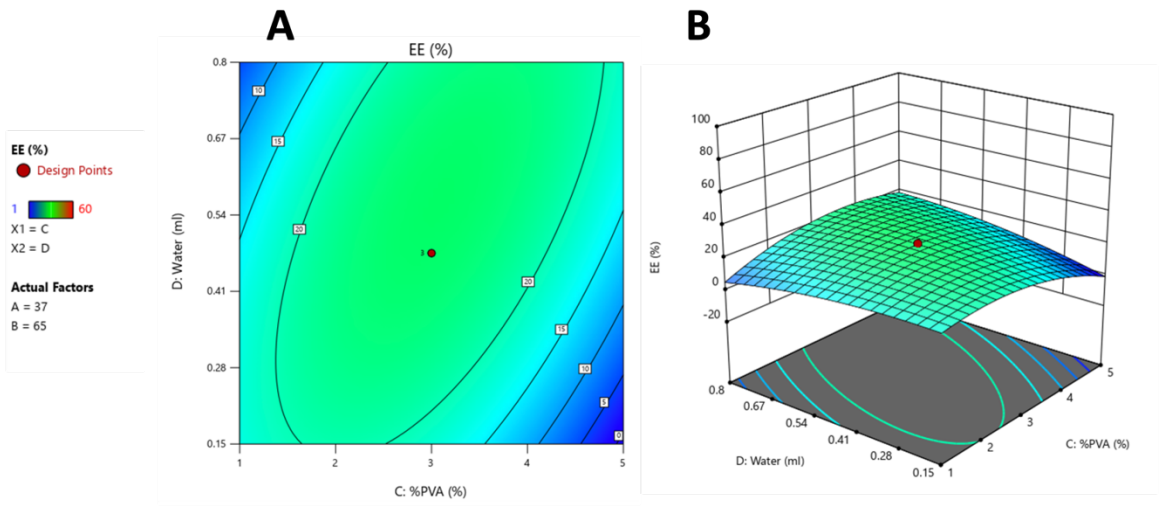


*Figure 14: (A)2D contour plot and (B) 3D response surface plot, respectively, illustrating the effect of water volume and %PVA on NP´s EE. The tone of blue denotes lower EE values, whereas the red color represents higher EE percentage.*

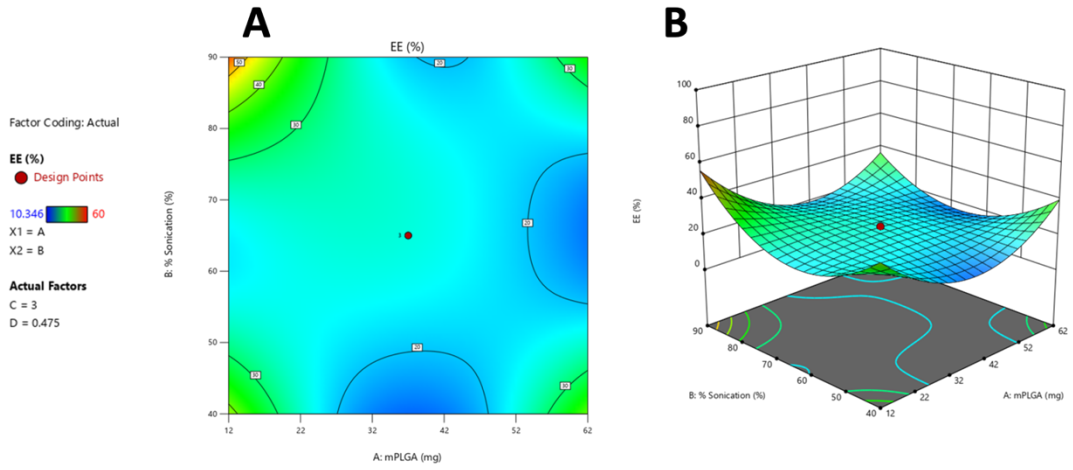


*Figure 15: (A)2D contour plot and (B) 3D response surface plot, respectively, illustrating the effect of PLGA mass and % of sonication on NP´s EE. The tone of blue denotes lower EE values, whereas the red color represents higher EE percentage.*

According to the regression equation (eq A3.10, Appendix 3), it can be concluded that PLGA mass negatively influence the EE of the NPs. By observation of the graphs of the figure 15 is possible to infer that by increasing the PLGA mass, the EE of the NPs decreases. As previously referred, a higher PLGA mass may result in the formation of larger NPs, leading to reduced surface area-to-volume ratio. This decreased surface area limits the availability of the encapsulation material for interaction and entrapment of the drug molecules, resulting in lower EE [132]. Contrarily, the amplitude sonication and water volume represent a positive effect on the EE of the NPs. Furthermore, for the same reason, increasing the amplitude of sonication result in the formation of monodisperse smaller NPs, which are more efficient at encapsulating the drug than polydisperse bigger particles [133]. Increased water volume leads to enhanced EE due to the reduced viscosity of the organic phase. This decreased viscosity facilitates the diffusion of drugs into the surrounding aqueous phase, minimizing any hindrance and allowing for a greater entrapment of drugs within the NPs[134].

## 4.3 Data Optimization and Model Validation

After establishing the constraints foreach response, the protocol was optimized. The NP size was selected to be between 140 and 180 nm, the PDI between 0.044 and 0.1, the zeta potential between -21.7 and -9.37 mV, and aiming the EE to target 60%. Table 6 illustrates the optimal experimental variables predicted by the software for each independent variable to fulfill the set response parameters.

*Table 6: Optimal value for each independent variable to obtain the optimal response.*

| Parameter | Independent Variable | Optimal Value |
|---|---|---|
| **X1** | PLGA mass (mg) | 12.12 |
| **X2** | % Sonication | 86 |
| **X3** | PVA (w/V %) | 4.66 |
| **X4** | Water Volume (mL) | 0.7293 |

To validate the proposed optimal protocol, five replicas of a checkpoint formulation were prepared using the optimal experimental values. The following Table 7 illustrates the predicted responses as well as the experimental outcomes.

*Table 7: Predicted responses and experimental outcomes.*

| | Predicted Value | Experimental Value |
|---|---|---|
| **Size (nm)** | **140** (123-158) | **141± 6** (135-147) |
| **PDI** | **0.07** (0.04-0.09) | **0.09 ± 0.01** (0.074-0.098) |
| **Zeta Potential (mV)** | **-19.6** (-21.4 - (-17.8)) | **-17.0 ± 0.8** (-17.8 – (-16.2)) |
| **EE (%)** | **60.0** (57.6-62.4) | **59.1 ± 9.2** (49.9-68.3) |

From Table 7, is possible to infer that all variables are within the expected range, except from the ZP which is slightly higher than expected. The produced NPs have appropriate physicochemical properties for brain delivery, with sizes less than 200 nm and PDI values below 0.1, representing a monodisperse sample. Despite, being outside of the predicted range, the produced NPs are still negatively charged as predicted. Also, the high absolute ZP values of the NPs, due to the negatively charged carboxyl groups of PLGA, indicate that the NPs are stable and with no risk of aggregation.

The high and favorable values representing the EE of the NPs indicate a successful drug entrapment within the NPs, suggesting an effective drug encapsulation.

## 4.4 Transferrin conjugation with CHQ loaded PLGA NPs

For an active targeting drug delivery strategy, Tf was used to conjugate the CHQ loaded PLGA NPs. The CE was assessed by quantifying the unbound Tf using the BCA kit.

The CE obtained was considerably favorable with values around (78.6± 1.2%) , correspondent to 157 ± 2 molecules of Tf per NP.

The NPs were physiochemically characterized, and the results are represented in Table 8, such as non-modified NPs, in order to simplify the comparison between the non-modified and Tf-modified NPs.

*Table 8: Physiochemical characteristics of non-conjugated NPs and Tf-conjugated NPs.*

| | Non-conjugated NPs | Tf-conjugated NPs |
|---|---|---|
| **Size (nm)** | 141± 6 | 140 ± 8 |
| **PDI** | 0.09 ± 0.01 | 0.09 ± 0.02 |
| **Zeta Potential (mV)** | -17.0 ± 0.8 | -19.7 ± 2.3 |
| **EE (%)** | 59.1 ± 9.2 | 53.2 ± 0.6 |

Based on the analysis of the table 8 results, it is feasible to conclude that Tf conjugation had no significant effect ($p>0.05$) on the physicochemical parameters of the NPs (size, PDI and zeta potential). However, a slight tendency to decrease de EE appears, the difference in the EE of Tf-conjugated NPs compared to non-conjugated NPs was not significant ($p>0.05$).

## 4.5 Transmission electron microscopy

TEM analysis provides insights into the morphology and size of the prepared NPs. Figure 16 illustrates the observed characteristics of the CHQ loaded PLGA NPs.

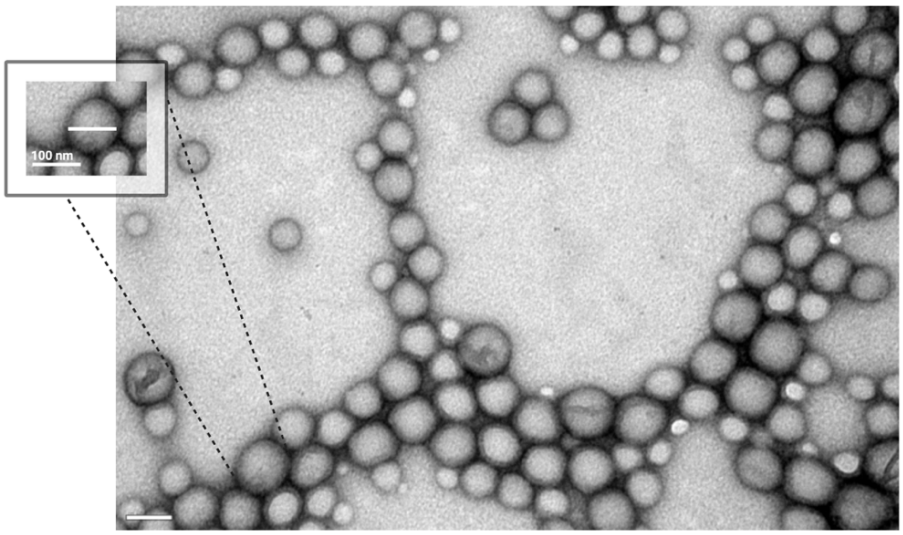


*Figure 16:TEM image of the prepared CHQ-loaded PLGA NPs. Scale bar 100 nm.*

Upon observing the NPs, it becomes evident that they exhibit a spherical and uniform shape, which aligns with the typical characteristics of polymeric NPs [135].

Although, it is noteworthy to mention that the size presented in the TEM analysis ($\pm 100$ nm) is slightly smaller than the size determined by using the DLS technique ($\pm 141$ nm). This is due to the fact that DLS provides the hydrodynamic size of the NPs, which includes the assembly of NPs and the surrounding electron-ion layer, instead of the real NPs size [136].

The analysis also revealed that the preparation process resulted in the formation of well-stabilized, uniformly distributed PLGA NPs. Thus, the spherical shape of the NPs and their consistent size distribution, indicates the predicted low PDI value (<0.1).

Furthermore, is also possible to observe a distinct dark perimeter surrounding the NPs, that possibly indicates the presence of a PVA coating.

Moreover, PVA micelles are also represented in the TEM figure, as smaller spheres with a lighter color, due to the fact that PLGA NPs are heavier that the PVA micelles, and consequently

PVA micelles exhibit a weaker electron scattering [137]. The observation of white micelles in the TEM image can provide valuable information about the distribution and behavior of surfactant molecules within the NPs formulation. In this case is possible to conclude that the optimal PVA percentage (4.66%) used was in excess, since not all PVA molecules were used to coat the produced NPs.

## 4.6 FTIR analysis

FTIR analysis was employed to confirm the effective conjugation of CHQ-loaded PLGA NPs with Tf. Control samples of CHQ-loaded unmodified PLGA NPs were also subjected to analysis. The obtained FTIR spectra are presented in Figures 17 and 18.

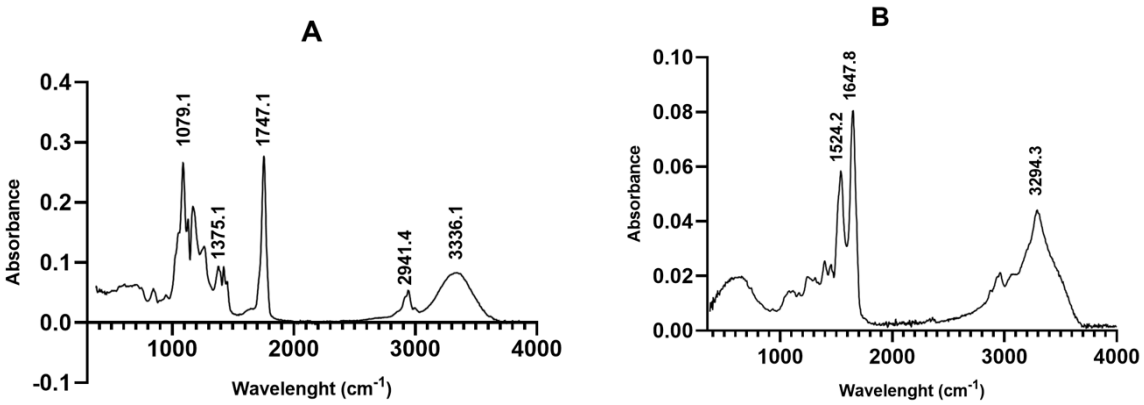


*Figure 17:FTIR absorbance spectrum of (A) CHQ-loaded PLGA NPs (control) (B) Tf stock solution within a wavenumber from 300-4000 $cm^{-1}$.*

According to literature, the PLGA spectrum showed characteristic peaks at 1079.1 $cm^{-1}$ indicative of C-O-C stretch peak; at 1375.1 $cm^{-1}$ representing the C-H bends; at 1747.1 $cm^{-1}$ indicative of C=O stretching (due to alpha-substitution); at 2941.4 $cm^{-1}$ representative of C-H stretching vibrations; and finally, at 3336.1 $cm^{-1}$ indicative of O-H end group [138].

In the absorbance spectrum of Tf, three distinct regions reveal prominent peaks that correspond to the amine groups within the Tf molecule. The first amine group is observed at approximately 1524.2 $cm^{-1}$, while the second amine group is represented by a peak at 1647.8 $cm^{-1}$, and the thirds amine corresponds to the 3294.3 $cm^{-1}$ peak [139, 140]. By analyzing Tf-CHQ-PLGA NPs specter Figure 18 it is possible to observe the two peaks corresponding to amine I and II of Tf, suggesting a successful conjugation. Additionally, a slight increase in those peaks, from 1524.2 to 1529.2 $cm^{-1}$, 1647.8 to 1656.7 $cm^{-1}$, and in the PLGA peak 1747.1 to 1751.2 $cm^{-1}$, in post-conjugation specter is also evident, which implies that the molecules have a higher physical interaction.

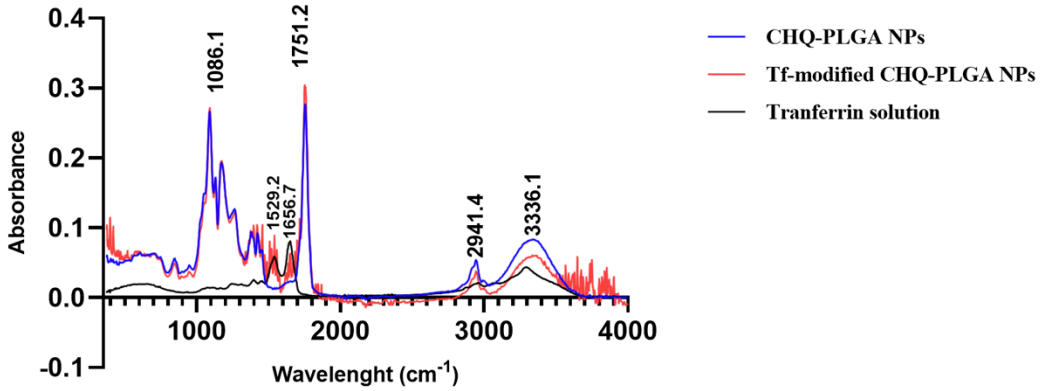


*Figure 18: FTIR absorbance spectrum of Tf solution, CHQ-loaded PLGA NPs and Tf-conjugated CHQ-loaded PLGA NPs*

By observation of the post-conjugation specter is possible to conclude that the Tf conjugation was successfully accomplished.

## 4.7 CHQ Release Profile

One of the key features of DDSs is the capacity of nanocarriers to sustainably release the encapsulated drugs. As a result, the produced Tf-conjugated and non-conjugated PLGA NPs were evaluated for their capacity to sustain the CHQ release. The *in vitro* release profile of CHQ from PLGA NPs was investigated under physiologically relevant settings such as temperature, pH, and salt concentrations (37°C in PBS, pH 7.4, 0.01M) and are illustrated on the following figure 19.

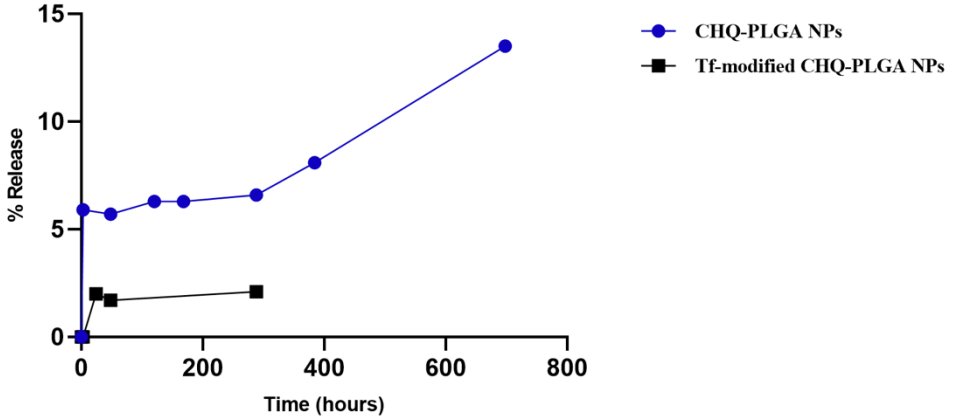


*Figure 19: in vitro release profile of CHQ from CHQ-loaded PLGA NPs and Tf-conjugated CHQ-loaded PLGA NPs*

Drug release from PLGA NPs can occur by different mechanisms. Usually, there is evidence of three distinct phases in the release profile over time. These phases include an initial burst phase, a lag phase, and a subsequent release of the drug following the lag phase. It is important to note that the release during the lag phase is, commonly associated with the loss of polymer mass rather than a decrease in the molecular weight of the polymer [141]. By observation of the release profile of non-modified PLGA NPs, represented in figure 19, the predicted initial burst phase is well-

established since there was a release of 5.9% during the first three hours. Subsequently, it was verified a slower increase of the percentage of drug released during the following 285 hours. The minimal rise observed, from 5.9% to 6.6%, provides evidence that the release profile during this specific period is consistent with the predicted lag phase. In this phase the drug release is commonly influenced by various mechanisms, including surface erosion of the polymer matrix, cleavage of polymer bonds at the surface or within the bulk of the matrix, and diffusion of the physically entrapped drug. However, it is common for drug release to occur through a simultaneous combination of all three mechanisms [142].

In the subsequent 410-hour period, there was almost twice the amount of drug released compared to the previous period, reaching a maximum of 13.5% over the entire 698-hour duration of the release experiment.

Regarding the release profile of Tf-modified CHQ-PLGA NPs the release was not successful comparing with the release profile of the non-modified NPs, since the maximum release percentage achieved was 2.1% until 264-hour period. Although it was also evident, in figure 19 the first two predicted phases, the initial burst phase and the following lag phase. The slower CHQ release observed in these NPs, may be explained by the fact that the Tf molecules attached to the NPs' surface can hinder the drug diffusion[143].

Although the CHQ was released at a slow and controlled rate, ideally the amount of drug released should have been higher, in order for it to be sufficiently efficient *in vivo*.

## 4.8 NPs Stability in storage conditions

To evaluate the long-term colloidal stability of CHQ-loaded PLGA NPs, various properties such as mean size, PDI, and ZP were weekly measured. The analysis aimed to assess the stability of the NPs when suspended in ultrapure water under storage conditions. The stability evaluation was conducted over a duration of three weeks, with samples stored at both 4°C and room temperature. The findings from these assessments are presented in tables 9 and 10, respectively. Table 11 represents the stability evaluation of Tf-conjugated CHQ-loaded PLGA NPs in storage conditions at 4ºC.

*Table 9:CHQ-loaded PLGA NPs characteristics in storage conditions at room temperature. Data is presented as mean value ± SD.*

| Time (weeks) | Size (nm) | PDI | ZP (mV) |
|---|---|---|---|
| **Room Temperature** | | | |
| **0** | 149 ± 2 | 0.22 ± 0.03 | - 21 ± 1 |
| **1** | 139 ± 3 | 0.09 ± 0.02 | - 22 ± 2 |
| **2** | 134 ± 1 | 0.08 ± 0.03 | - 22 ± 2 |
| **3** | 138 ± 0.2 | 0.10 ± 0.03 | - 22 ± 3 |

*Table 10:CHQ-loaded PLGA NPs characteristics in storage conditions at 4ºC. Data is presented as mean value ± SD.*

| Time (weeks) | Size | PDI | ZP |
|---|---|---|---|
| | | **4ºC** | |
| **0** | 144 ± 1 | 0.09 ± 0.02 | - 16.9 ± 0.9 |
| **1** | 152 ± 15 | 0.09 ± 0.07 | - 18 ± 2 |
| **2** | 160 ± 29 | 0.11 ± 0.08 | - 18 ± 3 |
| **3** | 156 ± 21 | 0.09 ± 0.07 | - 17 ± 2 |

*Table 11: Tf-conjugated CHQ-loaded PLGA NPs characteristics in storage conditions at 4ºC. Data is presented as mean value ± SD.*

| Time (weeks) | Size | PDI | ZP |
|---|---|---|---|
| | | **4ºC (Tf-conjugated NPs)** | |
| **0** | 140 ± 8 | 0.09 ± 0.02 | - 20 ± 2 |
| **1** | 140 ± 13 | 0.06 ± 0.02 | - 19.9 ± 0.1 |

At room temperature the NPs exhibited some significant variation of size and PDI ($p<0.05$. This may be related with degradation of the PLGA in water leading to the reduction of size. The variation of ZP was not significant ($p>0.05$).

At lower temperature both CHQ-loaded PLGA NPs and Tf-conjugated CHQ-loaded PLGA NPs were considered stable during the evaluation time since none of the studied characteristics represented significant changes overtime ($p>0.05$). This suggests that 4ºC is the most suitable temperature for NPs' storage.

## 4.9 NPs stability in simulated physiological conditions

Analogously, the mean size, PDI and zeta potential values of the NPs were measured weekly to evaluate their colloidal stability under physiological conditions. To simulate the physiological conditions, the CHQ-loaded PLGA NPs and Tf-modified CHQ-loaded PLGA NPs stability was evaluated on PBS medium (0.01 M) at pH 7.4. The obtained results are presented in tables 12 and 13.

*Table 12: CHQ-loaded PLGA NPs characteristics in storage conditions at 37ºC in PBS (7.4 PH). Data is presented for only one replica.*

| Time (hours) | Size | PDI | ZP |
|---|---|---|---|
| **37ºC in PBS (pH 7.4)** | | | |
| | | | |
| **(Non-modified NPs)** | | | |
| **0** | 141 | 0.09 | -4.5 |
| **3** | 141 | 0.04 | -1.8 |
| **24** | 146 | 0.07 | -1.7 |
| **48** | 143 | 0.06 | -2.0 |
| **120** | 143 | 0.05 | -2.6 |
| **168** | 144 | 0.05 | -2.1 |
| **288** | 141 | 0.06 | -2.5 |
| **384** | 139 | 0.07 | -2.6 |
| **530** | 135 | 0.05 | -3.1 |
| **698** | 133 | 0.05 | -3.1 |

*Table 13:Tf-conjugated CHQ-loaded PLGA NPs characteristics in storage conditions at 37ºC in PBS (7.4 PH). Data is presented for only one replica.*

| Time (hours) | Size | PDI | ZP |
|---|---|---|---|
| **37ºC in PBS (pH 7.4)** | | | |
| | | | |
| **(Tf-modified NPs)** | | | |
| **0** | 143 | 0.17 | -1.6 |
| **3** | 135 | 0.11 | -2.0 |
| **24** | 138 | 0.13 | -2.0 |
| **48** | 140 | 0.17 | -2.0 |
| **120** | 140 | 0.12 | -2.7 |

The results, summarized in tables 12 and 13, indicate that the NPs exhibited charges less negative comparing to the NPs suspended in ultrapure water. This can be attributed to the buffering effect of the PBS, which neutralizes the surface charges on the NPs. The interaction between the free charges present in the PBS and the negative charges on the NP´s surface leads to a zeta potential less negative and more near to zero when the particles are in suspension in PBS [144].

Additionally, both CHQ-loaded PLGA NPs and Tf-modified CHQ-loaded PLGA NPs were considered stable in PBS, since it appears all properties analyzed remain constant.

# 5 Conclusion

Over the last few decades, nanomedicine has emerged as a promising field in cancer research, offering solutions to the limitations of traditional approaches, such as intrinsic resistance mechanisms in GBM treatment of drugs like TMZ and the low bioavailability of the drug in the brain due to the presence of biological barriers.

Additionally, nanotechnology provides a breakthrough by using nano-sized particles for improved drug delivery and targeting of tumor tissues. This innovative approach holds the potential for significant advancements in cancer detection and treatment, providing hope for more effective therapies.

Thus, there is a new interest in repurposing non-alkylating drugs already approved by FDA such as CHQ for the treatment of GBM.

In this study was proposed a formulation to produce PLGA NPs loaded with CHQ, where all characteristics such as size, PDI and zeta potential were considered with the aim of promoting their ability to cross the BBB and ultimately to reach the tumor cells.

To obtain the optimal protocol for the production of NPs with desirable characteristics and EE, it was used the experimental design that proved to be efficient using CCD. A total of 27 formulations were prepared and the obtained model was successfully validated since the characteristics of the prepared NPs aligned with the outcomes predicted by the software. The developed optimal NPs had the desirable characteristics such as size ($141 \pm 6$ nm < 200 nm), PDI ($0.09 \pm 0.01$ <0.1) and ZP ($-17.0 \pm 0.8$ mV <0 mV). Furthermore, a relatively high encapsulation efficiency (EE) of approximately $59.1\% \pm 9.2$ was achieved.

In addition, to enhance their specificity the produced NPs underwent a conjugation process with Tf, which yielded NPs with about $157 \pm 2$ molecules of Tf on their surface.

The release profile of CHQ was examined, revealing that the NPs displayed a sustained and controlled release pattern. This profile was marked by a gradual and extended release of the drug over time. Although, the percentage of drug released (13.5% for non-conjugated and 2.1% for Tf-conjugated NPs) was not significant until the end of the study, the findings indicate the ability of the NPs to sustain the release of the drug in a controlled manner.

The stability of the prepared NPs was also studied under both storage and physiological conditions. Despite at room temperature the NPs exhibited some significant variation of size and PDI, at lower temperature (4ºC), both non-modified and Tf-conjugated CHQ-loaded PLGA NPs were considered stable during the evaluation time. In physiological conditions NPs exhibited charges less negative comparing to the NPs suspended in ultrapure water because of the buffering effect of the PBS, however they remained stable during the experiment.

To corroborate the purpose of this study, additional experiments are needed to assess the nanosystem efficacy. In this regard, further release studies can be conducted to achieve a higher percentage of drug released while ensuring sufficient efficacy *in vivo*.

In prospective investigations, cellular studies and *in vivo* experiments to enhance the understanding of the developed NPs' performance can be conducted.

Through the implementation of these further studies, significant insights into the efficacy and functionality of the proposed nanosystem can be acquired and may lead to the expansion of its potential applications in the scientific community.

# 6 Assessment of the work done

## 6.1 Objectives Achieved

The main objective of this study was to develop PLGA NPs loaded with CHQ for GBM treatment and improve their efficacy using experimental techniques. The aim was to achieve targeted delivery of CHQ by modifying PLGA NPs with Tf. Additionally, the study aimed to evaluate the controlled release of the drug under storage conditions and normal physiological conditions.

Firstly, the development of CHQ-PLGA NPs was well accomplished since it was possible to obtain a reasonable concentration of CHQ encapsulated. The resulting NPs exhibited favorable characteristics that make them suitable for addressing challenges such as crossing the BBB. The experimental design was successfully accomplished since it was possible to validate the model and consequently to obtain NPs with the intended size <200 nm, low PDI values, negative ZP and considerably high EE (around 60%).

Subsequently, with the aim to develop NPs with higher specificity, the NPs were successfully conjugated with Tf.

Finally, CHQ release was considered controlled and sustained, however the percentage of CHQ release was still relatively low, consequently more studies should be done to achieve a higher percentage of release.

## 6.2 Final Assessment

In my sincere opinion, my dissertation project on the development of NPs for delivering CHQ in the treatment of GBM was a remarkable milestone in my academic path. GBM, with its aggressive nature and limited treatment options, has touched the lives of many, and I am driven by a deep personal desire to make a difference.

This journey was a rollercoaster ride, exposing me to the realities behind the development of the medicines we rely on. Was filled with good days where the results were what was expected, but mostly filled with bad days were the obtained results were not near the expected ones, and I had to try again and again through the days after. Although it was that bad days that lead me to learn even more and to understand what was wrong and why.

Throughout this process, I have gained a deep understanding of the challenges and complexities involved in treating GBM. By focusing on NPs as carriers for CHQ, I have embraced an innovative approach that has the potential to revolutionize current treatment methods. This personalized approach to drug delivery holds tremendous promise in improving the efficacy and targeting of treatment for GBM patients. Undoubtedly, further effort and dedication are required to attain remarkable accomplishments.

This work has provided me with a newfound realization of the significant role that Chemical Engineering and Biotechnology plays in addressing various challenges across the world.

In conclusion, I am filled with excitement and optimism as I move forward with the conviction that my work on developing NPs for delivering CHQ in GBM treatment has the potential to shape the future of healthcare and bring about meaningful change.

# 7 References


1. Yasaswi, P.S., K. Shetty, and K.S. Yadav, *Temozolomide nano enabled medicine: promises made by the nanocarriers in glioblastoma therapy.* Journal of Controlled Release, 2021. **336**: p. 549-571.

2. Ostrom, Q.T., et al., *CBTRUS Statistical Report: Primary brain and other central nervous system tumors diagnosed in the United States in 2010-2014.* Neuro Oncol, 2017. **19**(suppl_5): p. v1-v88.

3. Ovejero-Sánchez, M., R. González-Sarmiento, and A.B. Herrero, *Synergistic effect of Chloroquine and Panobinostat in ovarian cancer through induction of DNA damage and inhibition of DNA repair.* Neoplasia, 2021. **23**(5): p. 515-528.

4. Aldoghachi, A.F., et al., *Recent Advances in the Therapeutic Strategies of Glioblastoma Multiforme.* Neuroscience, 2022. **491**: p. 240-270.

5. Mujokoro, B., et al., *Nano-structures mediated co-delivery of therapeutic agents for glioblastoma treatment: A review.* Materials Science and Engineering: C, 2016. **69**: p. 1092-1102.

6. Wu, W., et al., *Glioblastoma multiforme (GBM): An overview of current therapies and mechanisms of resistance.* Pharmacological Research, 2021. **171**: p. 105780.

7. Khan, I., et al., *Nanomedicine for glioblastoma: Progress and future prospects.* Seminars in Cancer Biology, 2022. **86**: p. 172-186.

8. Whitfield, B.T. and J.T. Huse, *Classification of adult-type diffuse gliomas: Impact of the World Health Organization 2021 update.* Brain Pathology, 2022. **32**(4): p. e13062.

9. Kapoor, M.K.G., Vikas *Astrocytoma.* NCBI Bookshelf, 2022 Oct 3.

10. Morgan, L.L., *The epidemiology of glioma in adults: a "state of the science" review.* Neuro Oncol, 2015. **17**(4): p. 623-4.

11. Ostrom, Q.T., et al., *Epidemiology of Intracranial Gliomas.* Prog Neurol Surg, 2018. **30**: p. 1-11.

12. Ohgaki, H. and P. Kleihues, *The definition of primary and secondary glioblastoma.* Clin Cancer Res, 2013. **19**(4): p. 764-72.

13. Louis, D.N., et al., *The 2016 World Health Organization Classification of Tumors of the Central Nervous System: a summary.* Acta Neuropathol, 2016. **131**(6): p. 803-20.

14. Ceccarelli, M., et al., *Molecular Profiling Reveals Biologically Discrete Subsets and Pathways of Progression in Diffuse Glioma.* Cell, 2016. **164**(3): p. 550-563.

15. Ellingson, B.M., et al., *Consensus recommendations for a standardized Brain Tumor Imaging Protocol in clinical trials.* Neuro Oncol, 2015. **17**(9): p. 1188-98.

16. Stupp, R., et al., *Radiotherapy plus Concomitant and Adjuvant Temozolomide for Glioblastoma.* New England Journal of Medicine, 2005. **352**(10): p. 987-996.

17. Altwairgi, A.K., et al., *Management and treatment recommendations for World Health Organization Grade III and IV gliomas.* Int J Health Sci (Qassim), 2017. **11**(3): p. 54-62.

18. Chaul-Barbosa, C. and D.F. Marques, *How We Treat Recurrent Glioblastoma Today and Current Evidence.* Current Oncology Reports, 2019. **21**(10): p. 94.

19. Alifieris, C. and D.T. Trafalis, *Glioblastoma multiforme: Pathogenesis and treatment.* Pharmacology & Therapeutics, 2015. **152**: p. 63-82.

20. Delello Di Filippo, L., et al., *Improving temozolomide biopharmaceutical properties in glioblastoma multiforme (GBM) treatment using GBM-targeting nanocarriers.* European Journal of Pharmaceutics and Biopharmaceutics, 2021. **168**: p. 76-89.

21. Wesolowski, J.R., P. Rajdev, and S.K. Mukherji, *Temozolomide (Temodar).* American Journal of Neuroradiology, 2010. **31**(8): p. 1383-1384.

22. Stupp, R., et al., *Effect of Tumor-Treating Fields Plus Maintenance Temozolomide vs Maintenance Temozolomide Alone on Survival in Patients With Glioblastoma: A Randomized Clinical Trial.* JAMA, 2017. **318**(23): p. 2306-2316.

23. Yu, W., et al., *O6-Methylguanine-DNA Methyltransferase (MGMT): Challenges and New Opportunities in Glioma Chemotherapy.* Frontiers in Oncology, 2020. **9**.

24. Taylor, J.W. and D. Schiff, *Treatment Considerations for MGMT-Unmethylated Glioblastoma.* Current Neurology and Neuroscience Reports, 2014. **15**(1): p. 507.

25. Raj, D., et al., *Pharmacological strategies for improving the prognosis of glioblastoma.* Expert Opinion on Pharmacotherapy, 2021. **22**(15): p. 2019-2031.

26. Cha, G.D., et al., *Advances in drug delivery technology for the treatment of glioblastoma multiforme.* Journal of Controlled Release, 2020. **328**: p. 350-367.

27. Reardon, D.A., *Principles of Neuro-Oncology.* Neuro-Oncology, 2006. **8**(2): p. 194-194.

28. Zhang, D.Y., et al., *Ultrasound-mediated Delivery of Paclitaxel for Glioma: A Comparative Study of Distribution, Toxicity, and Efficacy of Albumin-bound Versus Cremophor Formulations.* Clinical Cancer Research, 2020. **26**(2): p. 477-486.

29. Patel, R., et al., *Epigenetic silencing of telomerase and a non-alkylating agent as a novel therapeutic approach for glioma.* Brain Research, 2008. **1188**: p. 173-181.

30. Jiang, P., et al., *Novel anti-glioblastoma agents and therapeutic combinations identified from a collection of FDA approved drugs.* Journal of Translational Medicine, 2014. **12**(1): p. 13.

31. García-Serradilla, M., C. Risco, and B. Pacheco, *Drug repurposing for new, efficient, broad spectrum antivirals.* Virus Research, 2019. **264**: p. 22-31.

32. Thomé, R., et al., *Chloroquine: Modes of action of an undervalued drug.* Immunology Letters, 2013. **153**(1): p. 50-57.

33. Jiang, X., et al., *Role of the tumor microenvironment in PD-L1/PD-1-mediated tumor immune escape.* Molecular Cancer, 2019. **18**(1): p. 10.

34. Viry, E., et al., *Autophagy: An adaptive metabolic response to stress shaping the antitumor immunity.* Biochemical Pharmacology, 2014. **92**(1): p. 31-42.

35. Kimura, T., et al., *Chloroquine in Cancer Therapy: A Double-Edged Sword of Autophagy.* Cancer Research, 2013. **73**(1): p. 3-7.

36. Weyerhäuser, P., S.R. Kantelhardt, and E.L. Kim, *Re-purposing Chloroquine for Glioblastoma: Potential Merits and Confounding Variables.* Frontiers in Oncology, 2018. **8**.

37. Amaravadi, R.K., et al., *Autophagy inhibition enhances therapy-induced apoptosis in a Myc-induced model of lymphoma.* J Clin Invest, 2007. **117**(2): p. 326-36.

38. Eng, C.H., et al., *Macroautophagy is dispensable for growth of KRAS mutant tumors and chloroquine efficacy.* Proc Natl Acad Sci U S A, 2016. **113**(1): p. 182-7.

39. King, M.A., I.G. Ganley, and V. Flemington, *Inhibition of cholesterol metabolism underlies synergy between mTOR pathway inhibition and chloroquine in bladder cancer cells.* Oncogene, 2016. **35**(34): p. 4518-28.

40. Maes, H., et al., *Tumor Vessel Normalization by Chloroquine Independent of Autophagy.* Cancer Cell, 2014. **26**(2): p. 190-206.

41. Zhou, W., et al., *Chloroquine against malaria, cancers and viral diseases.* Drug Discovery Today, 2020. **25**(11): p. 2012-2022.

42. Lee, A.H., L.S. Symington, and D.A. Fidock, *DNA Repair Mechanisms and Their Biological Roles in the Malaria Parasite Plasmodium falciparum.* Microbiology and Molecular Biology Reviews, 2014. **78**(3): p. 469-486.

43. Bieging, K.T., S.S. Mello, and L.D. Attardi, *Unravelling mechanisms of p53-mediated tumour suppression.* Nat Rev Cancer, 2014. **14**(5): p. 359-70.

44. Kim, E.L., et al., *Chloroquine activates the p53 pathway and induces apoptosis in human glioma cells.* Neuro Oncol, 2010. **12**(4): p. 389-400.

45. Zhou, Q., M.A. McCracken, and J.S. Strobl, *Control of mammary tumor cell growth in vitro by novel cell differentiation and apoptosis agents.* Breast Cancer Res Treat, 2002. **75**(2): p. 107-17.

46. Lee, S.W., et al., *The synergistic effect of combination temozolomide and chloroquine treatment is dependent on autophagy formation and p53 status in glioma cells.* Cancer Lett, 2015. **360**(2): p. 195-204.

47. Loehberg, C.R., et al., *Ataxia telangiectasia-mutated and p53 are potential mediators of chloroquine-induced resistance to mammary carcinogenesis.* Cancer Res, 2007. **67**(24): p. 12026-33.

48. Maclean, K.H., et al., *Targeting lysosomal degradation induces p53-dependent cell death and prevents cancer in mouse models of lymphomagenesis.* J Clin Invest, 2008. **118**(1): p. 79-88.

49. Viallard, C. and B. Larrivée, *Tumor angiogenesis and vascular normalization: alternative therapeutic targets.* Angiogenesis, 2017. **20**(4): p. 409-426.

50. Roy, L.-O., M.-B. Poirier, and D. Fortin, *Chloroquine inhibits the malignant phenotype of glioblastoma partially by suppressing TGF-beta.* Investigational New Drugs, 2015. **33**(5): p. 1020-1031.

51. Li, Q., et al., *Chloroquine inhibits tumor growth and angiogenesis in malignant pleural effusion.* Tumour Biol, 2016.

52. Briceño, E., S. Reyes, and J. Sotelo, *Therapy of glioblastoma multiforme improved by the antimutagenic chloroquine.* Neurosurg Focus, 2003. **14**(2): p. e3.

53. Sotelo, J., E. Briceño, and M.A. López-González, *Adding chloroquine to conventional treatment for glioblastoma multiforme: a randomized, double-blind, placebo-controlled trial.* Ann Intern Med, 2006. **144**(5): p. 337-43.

54. J., S., *Chloroquine for Treatment of Glioblastoma Multiforme* in *U.S. National Library of Medicine*. (2009).

55. Verbaanderd, C., et al., *Repurposing Drugs in Oncology (ReDO)-chloroquine and hydroxychloroquine as anti-cancer agents.* Ecancermedicalscience, 2017. **11**: p. 781.

56. C., K., *International Cooperative Phase III Trial of the HIT-HGG Study Group (HIT-HGG-2013) (HIT-HGG-2013)*. 2018: U.S. National Library of Medicine.

57. Lambin P, C.I., Eekers D. , *The Addition of Chloroquine to Chemoradiation for Glioblastoma* U.S. National Library of Medicine, 2018.

58. De Ruysscher D, C.I., Eekers D. , *The Addition of Chloroquine to Chemoradiation for Glioblastoma (CHLOROBRAIN)* U.S. National Library of Medicine, 2018.

59. A., D., *IDO2 Genetic Status Informs the Neoadjuvant Efficacy of Chloroquine (CQ) in Brain Metastasis Radiotherapy.* U.S. National Library of Medicine 2015.

60. Raines, M.F., S.K. Bhargava, and E.S. Rosen, *The blood-retinal barrier in chloroquine retinopathy.* Investigative Ophthalmology & Visual Science, 1989. **30**(8): p. 1726-1731.

61. Blignaut, M., et al., *Revisiting the Cardiotoxic Effect of Chloroquine.* Cardiovascular Drugs and Therapy, 2019. **33**(1): p. 1-11.

62. Zhao, Y., et al., *Serious Cardiovascular Adverse Events Associated with Hydroxychloroquine/Chloroquine Alone or with Azithromycin in Patients with COVID-19: A Pharmacovigilance Analysis of the FDA Adverse Event Reporting System (FAERS).* Drugs Real World Outcomes, 2022. **9**(2): p. 231-241.

63. Compter, I., et al., *Chloroquine combined with concurrent radiotherapy and temozolomide for newly diagnosed glioblastoma: a phase IB trial.* Autophagy, 2021. **17**(9): p. 2604-2612.

64. Wang, X., J. Lee, and C. Xie, *Autophagy Regulation on Cancer Stem Cell Maintenance, Metastasis, and Therapy Resistance.* Cancers (Basel), 2022. **14**(2).

65. Shao, M., et al., *Encapsulation of chloroquine and doxorubicin by MPEG-PLA to enhance anticancer effects by lysosomes inhibition in ovarian cancer.* Int J Nanomedicine, 2018. **13**: p. 8231-8245.

66. Stevens, D.M., R.M. Crist, and S.T. Stern, *Nanomedicine Reformulation of Chloroquine and Hydroxychloroquine.* Molecules, 2020. **26**(1).

67. Wolfram, J., et al., *Safety of Nanoparticles in Medicine.* Curr Drug Targets, 2015. **16**(14): p. 1671-81.

68. Tang, L., et al., *Advanced and Innovative Nano-Systems for Anticancer Targeted Drug Delivery.* Pharmaceutics, 2021. **13**(8): p. 1151.

69. Zain, M., et al., *Chapter 10 - Applications of nanotechnology in biological systems and medicine*, in *Nanotechnology for Hematology, Blood Transfusion, and Artificial Blood*, A. Denizli, et al., Editors. 2022, Elsevier. p. 215-235.

70. Pérez-Herrero, E. and A. Fernández-Medarde, *Advanced targeted therapies in cancer: Drug nanocarriers, the future of chemotherapy.* Eur J Pharm Biopharm, 2015. **93**: p. 52-79.

71. Pearce, A.K. and R.K. O'Reilly, *Insights into Active Targeting of Nanoparticles in Drug Delivery: Advances in Clinical Studies and Design Considerations for Cancer Nanomedicine.* Bioconjug Chem, 2019. **30**(9): p. 2300-2311.

72. Grodzinski, P., et al., *Integrating Nanotechnology into Cancer Care.* ACS Nano, 2019. **13**(7): p. 7370-7376.

73. Ilinskaya, A.N. and M.A. Dobrovolskaia, *Nanoparticles and the blood coagulation system. Part II: safety concerns.* Nanomedicine (Lond), 2013. **8**(6): p. 969-81.

74. Sánchez-López, E., et al., *Memantine loaded PLGA PEGylated nanoparticles for Alzheimer's disease: in vitro and in vivo characterization.* Journal of Nanobiotechnology, 2018. **16**(1): p. 32.

75. Rizvi, S.A.A. and A.M. Saleh, *Applications of nanoparticle systems in drug delivery technology.* Saudi Pharmaceutical Journal, 2018. **26**(1): p. 64-70.

76. Rizvi, S.A.A. and A.M. Saleh, *Applications of nanoparticle systems in drug delivery technology.* Saudi Pharm J, 2018. **26**(1): p. 64-70.

77. Wohlfart, S., S. Gelperina, and J. Kreuter, *Transport of drugs across the blood–brain barrier by nanoparticles.* Journal of Controlled Release, 2012. **161**(2): p. 264-273.

78. Li, Y. and H. Zhang, *Nanoparticle-Based Drug Delivery Systems for Enhanced Tumor-Targeting Treatment.* J Biomed Nanotechnol, 2019. **15**(1): p. 1-27.

79. Morshed, M. and E.H. Chowdhury, *Gene Delivery and Clinical Applications*, in *Encyclopedia of Biomedical Engineering*, R. Narayan, Editor. 2019, Elsevier: Oxford. p. 345-351.

80. Alasvand, N., et al., *Chapter 13 - Therapeutic Nanoparticles for Targeted Delivery of Anticancer Drugs*, in *Multifunctional Systems for Combined Delivery, Biosensing and Diagnostics*, A.M. Grumezescu, Editor. 2017, Elsevier. p. 245-259.

81. Pelicano, H., et al., *Glycolysis inhibition for anticancer treatment.* Oncogene, 2006. **25**(34): p. 4633-4646.

82. Gao, W., J.M. Chan, and O.C. Farokhzad, *pH-Responsive nanoparticles for drug delivery.* Mol Pharm, 2010. **7**(6): p. 1913-20.

83. Pandit, R., L. Chen, and J. Götz, *The blood-brain barrier: Physiology and strategies for drug delivery.* Adv Drug Deliv Rev, 2020. **165-166**: p. 1-14.

84. Zhan, C. and W. Lu, *The blood-brain/tumor barriers: challenges and chances for malignant gliomas targeted drug delivery.* Current pharmaceutical biotechnology, 2012. **13**(12): p. 2380-2387.

85. Tian, H., et al., *Enhancing the therapeutic efficacy of nanoparticles for cancer treatment using versatile targeted strategies.* Journal of Hematology & Oncology, 2022. **15**(1): p. 132.

86. Danhier, F., *To exploit the tumor microenvironment: Since the EPR effect fails in the clinic, what is the future of nanomedicine?* Journal of Controlled Release, 2016. **244**: p. 108-121.

87. Zhang, P., et al., *Transferrin-Modified c[RGDfK]-Paclitaxel Loaded Hybrid Micelle for Sequential Blood-Brain Barrier Penetration and Glioma Targeting Therapy.* Molecular Pharmaceutics, 2012. **9**(6): p. 1590-1598.

88. Dixit, S., et al., *Transferrin receptor-targeted theranostic gold nanoparticles for photosensitizer delivery in brain tumors.* Nanoscale, 2015. **7**(5): p. 1782-1790.

89. Rashidzadeh, H., et al., *Targeted co-delivery of methotrexate and chloroquine via a pH/enzyme-responsive biocompatible polymeric nanohydrogel for colorectal cancer treatment.* Journal of Biomaterials Science, Polymer Edition, 2023: p. 1-19.

90. Gao, M., Y. Xu, and L. Qiu, *Enhanced combination therapy effect on paclitaxel-resistant carcinoma by chloroquine co-delivery via liposomes.* Int J Nanomedicine, 2015. **10**: p. 6615-32.

91. Panagiotaki, K.N., et al., *A Triphenylphosphonium-Functionalized Mitochondriotropic Nanocarrier for Efficient Co-Delivery of Doxorubicin and Chloroquine and Enhanced Antineoplastic Activity.* Pharmaceuticals (Basel), 2017. **10**(4).

92. Stagni, V., et al., *Targeting breast cancer stem-like cells using chloroquine encapsulated by a triphenylphosphonium-functionalized hyperbranched polymer.* International Journal of Pharmaceutics, 2020. **585**: p. 119465.

93. Yang, C., et al., *Facile Construction of Chloroquine Containing PLGA-Based pDNA Delivery System for Efficient Tumor and Pancreatitis Targeting in Vitro and in Vivo.* Mol Pharm, 2015. **12**(6): p. 2167-79.

94. Zhang, X., et al., *Investigation and intervention of autophagy to guide cancer treatment with nanogels.* Nanoscale, 2017. **9**(1): p. 150-163.

95. Sun, J.-H., et al., *Co-delivery nanoparticles of doxorubicin and chloroquine for improving the anti-cancer effect in vitro.* Nanotechnology, 2019. **30**(8): p. 085101.

96. Zhao, L., et al., *Co-delivery of Gefitinib and chloroquine by chitosan nanoparticles for overcoming the drug acquired resistance.* J Nanobiotechnology, 2015. **13**: p. 57.

97. Peng, J., et al., *Targeted Lipid Nanoparticles Encapsulating Dihydroartemisinin and Chloroquine Phosphate for Suppressing the Proliferation and Liver Metastasis of Colorectal Cancer.* Front Pharmacol, 2021. **12**: p. 720777.

98. Wang, D., et al., *A Polyoxometalate-Encapsulated Metal-Organic Framework Nanoplatform for Synergistic Photothermal-Chemotherapy and Anti-Inflammation of Ovarian Cancer.* Molecules, 2022. **27**(23).

99. Joshi, P., et al., *The anticancer activity of chloroquine-gold nanoparticles against MCF-7 breast cancer cells.* Colloids and Surfaces B: Biointerfaces, 2012. **95**: p. 195-200.

100. Matsumoto, S., et al., *Efficient pre-treatment for pancreatic cancer using chloroquine-loaded nanoparticles targeting pancreatic stellate cells.* Oncol Lett, 2021. **22**(2): p. 633.

101. Bhattarai, S.R., et al., *Enhanced gene and siRNA delivery by polycation-modified mesoporous silica nanoparticles loaded with chloroquine.* Pharm Res, 2010. **27**(12): p. 2556-68.

102. Gilman, J., et al., *Statistical Design of Experiments for Synthetic Biology.* ACS Synthetic Biology, 2021. **10**(1): p. 1-18.

103. Sankha, B., *Central Composite Design for Response Surface Methodology and Its Application in Pharmacy*, in *Response Surface Methodology in Engineering Science*, K. Palanikumar, Editor. 2021, IntechOpen: Rijeka. p. Ch. 5.

104. Babick, F., *Chapter 3.2.1 - Dynamic light scattering (DLS)*, in *Characterization of Nanoparticles*, V.-D. Hodoroaba, W.E.S. Unger, and A.G. Shard, Editors. 2020, Elsevier. p. 137-172.

105. Carpenter, D.K., *Dynamic light scattering with applications to chemistry, biology, and physics (Berne, Bruce J.; Pecora, Robert)*. 1977, ACS Publications.

106. Falke, S. and C. Betzel, *Dynamic Light Scattering (DLS): Principles, Perspectives, Applications to Biological Samples.* Radiation in Bioanalysis: Spectroscopic Techniques and Theoretical Methods, 2019. **8**: p. 173-193.

107. Bhattacharjee, S., *DLS and zeta potential – What they are and what they are not?* Journal of Controlled Release, 2016. **235**: p. 337-351.

108. Carvalho, P.M., et al., *Application of Light Scattering Techniques to Nanoparticle Characterization and Development.* Frontiers in Chemistry, 2018. **6**.

109. Mäntele, W. and E. Deniz, *UV–VIS absorption spectroscopy: Lambert-Beer reloaded.* Spectrochimica Acta Part A: Molecular and Biomolecular Spectroscopy, 2017. **173**: p. 965-968.

110. Koneru, T., et al., *Transferrin: Biology and Use in Receptor-Targeted Nanotherapy of Gliomas.* ACS Omega, 2021. **6**(13): p. 8727-8733.

111. Jhaveri, A., et al., *Transferrin-targeted, resveratrol-loaded liposomes for the treatment of glioblastoma.* Journal of Controlled Release, 2018. **277**: p. 89-101.

112. Jose, S., et al., *Transferrin-Conjugated Docetaxel–PLGA Nanoparticles for Tumor Targeting: Influence on MCF-7 Cell Cycle.* Polymers, 2019. **11**(11): p. 1905.

113. Guide, U., *"Pierce TM BCA Protein Assay Kit,".* 2020. **no. 2161296**: p. pp. 0–3.

114. Novais, Â., et al., *Fourier transform infrared spectroscopy: unlocking fundamentals and prospects for bacterial strain typing.* European Journal of Clinical Microbiology & Infectious Diseases, 2019. **38**(3): p. 427-448.

115. Bacsik, Z., J. Mink, and G. Keresztury, *FTIR Spectroscopy of the Atmosphere. I. Principles and Methods.* Applied Spectroscopy Reviews, 2004. **39**(3): p. 295-363.

116. Mohamed, M.A., et al., *Chapter 1 - Fourier Transform Infrared (FTIR) Spectroscopy*, in *Membrane Characterization*, N. Hilal, et al., Editors. 2017, Elsevier. p. 3-29.

117. Campbell, J., et al., *Chapter 9 - Nanoparticle characterization techniques*, in *Nanoparticles for Biomedical Applications*, E.J. Chung, L. Leon, and C. Rinaldi, Editors. 2020, Elsevier. p. 129-144.

118. Tang, C.Y. and Z. Yang, *Chapter 8 - Transmission Electron Microscopy (TEM)*, in *Membrane Characterization*, N. Hilal, et al., Editors. 2017, Elsevier. p. 145-159.

119. Titus, D., E. James Jebaseelan Samuel, and S.M. Roopan, *Chapter 12 - Nanoparticle characterization techniques*, in *Green Synthesis, Characterization and Applications of Nanoparticles*, A.K. Shukla and S. Iravani, Editors. 2019, Elsevier. p. 303-319.

120. Moscardini, A., et al., *Uranium-free X solution: a new generation contrast agent for biological samples ultrastructure.* Scientific Reports, 2020. **10**(1): p. 11540.

121. Schuster, J., et al., *Tracking the physical stability of fluorescent-labeled mAbs under physiologic in vitro conditions in human serum and PBS.* European Journal of Pharmaceutics and Biopharmaceutics, 2020. **152**: p. 193-201.

122. Cho, E.J., et al., *Nanoparticle Characterization: State of the Art, Challenges, and Emerging Technologies.* Molecular Pharmaceutics, 2013. **10**(6): p. 2093-2110.

123. Hoshyar, N., et al., *The effect of nanoparticle size on in vivo pharmacokinetics and cellular interaction.* Nanomedicine (Lond), 2016. **11**(6): p. 673-92.

124. Meng, Q., et al., *Influence of nanoparticle size on blood–brain barrier penetration and the accumulation of anti-seizure medicines in the brain.* Journal of Materials Chemistry B, 2022. **10**(2): p. 271-281.

125. Chatterjee, M. and N. Chanda, *Formulation of PLGA nano-carriers: specialized modification for cancer therapeutic applications.* Materials Advances, 2022. **3**(2): p. 837-858.

126. Liu, Y., J. Pan, and S.S. Feng, *Nanoparticles of lipid monolayer shell and biodegradable polymer core for controlled release of paclitaxel: effects of surfactants on particles size, characteristics and in vitro performance.* Int J Pharm, 2010. **395**(1-2): p. 243-50.

127. Clayton, K.N., et al., *Physical characterization of nanoparticle size and surface modification using particle scattering diffusometry.* Biomicrofluidics, 2016. **10**(5): p. 054107.

128. Tefas, L.R., et al., *Development and optimization of quercetin-loaded PLGA nanoparticles by experimental design.* Clujul Med, 2015. **88**(2): p. 214-23.

129. Heshmati Aghda, N., et al., *High Throughput Preparation of Poly(Lactic-Co-Glycolic Acid) Nanoparticles Using Fiber Fluidic Reactor.* Materials, 2020. **13**(14): p. 3075.

130. Shao, X.R., et al., *Independent effect of polymeric nanoparticle zeta potential/surface charge, on their cytotoxicity and affinity to cells.* Cell Prolif, 2015. **48**(4): p. 465-74.

131. Kalaji, N., et al., *Colloidal and physicochemical characterization of proteincontaining poly(lactide-co-glycolide) (PLGA) microspheres before and after drying.* e-Polymers, 2009. **9**(1).

132. Hajj Ali, H., et al., *Shea butter solid nanoparticles for curcumin encapsulation: Influence of nanoparticles size on drug loading.* European Journal of Lipid Science and Technology, 2016. **118**(8): p. 1168-1178.

133. Shaikh, M.V., M. Kala, and M. Nivsarkar, *Formulation and optimization of doxorubicin loaded polymeric nanoparticles using Box-Behnken design: ex-vivo stability and in-vitro activity.* European Journal of Pharmaceutical Sciences, 2017. **100**: p. 262-272.

134. Madani, F., et al., *Investigation of effective parameters on size of paclitaxel loaded PLGA nanoparticles.* Advanced pharmaceutical bulletin, 2018. **8**(1): p. 77.

135. Visaveliya, N. and J.M. Köhler, *Control of Shape and Size of Polymer Nanoparticles Aggregates in a Single-Step Microcontinuous Flow Process: A Case of Flower and Spherical Shapes.* Langmuir, 2014. **30**(41): p. 12180-12189.

136. Kuznetsova, E.V., et al., *The Role of Integrated Approach in the Determination of Nanoparticle Sizes in Dispersions.* Colloid Journal, 2022. **84**(6): p. 704-714.

137. Franken, L.E., et al., *A Technical Introduction to Transmission Electron Microscopy for Soft-Matter: Imaging, Possibilities, Choices, and Technical Developments.* Small, 2020. **16**(14): p. 1906198.

138. Singh, G., et al., *Recent biomedical applications and patents on biodegradable polymer-PLGA.* International Journal of Pharmacology and Pharmaceutical Sciences, 2014. **1**: p. 30-42.

139. Frasco, M.F., et al., *Transferrin surface-modified PLGA nanoparticles-mediated delivery of a proteasome inhibitor to human pancreatic cancer cells.* Journal of Biomedical Materials Research Part A, 2015. **103**(4): p. 1476-1484.

140. Soe, Z.C., et al., *Transferrin-Conjugated Polymeric Nanoparticle for Receptor-Mediated Delivery of Doxorubicin in Doxorubicin-Resistant Breast Cancer Cells.* Pharmaceutics, 2019. **11**(2): p. 63.

141. Corrigan, O.I. and X. Li, *Quantifying drug release from PLGA nanoparticulates.* European Journal of Pharmaceutical Sciences, 2009. **37**(3): p. 477-485.

142. Langer, R.S. and N.A. Peppas, *Present and future applications of biomaterials in controlled drug delivery systems.* Biomaterials, 1981. **2**(4): p. 201-214.

143. Gupta, Y., A. Jain, and S.K. Jain, *Transferrin-conjugated solid lipid nanoparticles for enhanced delivery of quinine dihydrochloride to the brain.* Journal of Pharmacy and Pharmacology, 2010. **59**(7): p. 935-940.

144. Bihari, P., et al., *Optimized dispersion of nanoparticles for biological in vitro and in vivo studies.* Particle and Fibre Toxicology, 2008. **5**(1): p. 14.

145. Joshi, P., et al., *Binding of chloroquine–conjugated gold nanoparticles with bovine serum albumin.* Journal of Colloid and Interface Science, 2011. **355**(2): p. 402-409.

# 8 Appendix

## A1. Context and State of the Art

*Table A1. 1: Nanosystems for the delivery of CHQ for the treatment of different types of oncologic diseases.*

| Nanocarrier | Coating | Targeting moiety | Co-loaded cargo | Size (nm) | Surface charge | Application | Cell/animal model | Main conclusions | Ref. |
|---|---|---|---|---|---|---|---|---|---|
| PMA nanohydrogel | n.a. | Methotrexate | Methotrexate | 174 | Negative | Colorectal cancer | Human colon cancer cells (SW480), healthy mice (Swiss albino) | The pH/enzyme-responsive NPs enhanced the antiproliferative activity of CHQ. The NPs proved to be biocompatible *in vitro* and *in vivo*. | [89] |
| PLA NPs | M-PEG | n.a. | DOX | 25 | Negative | Ovarian cancer | DOX-resistant (A2780 and SKOV3) and non-resistant (A2780/DOXR) human ovarian cancer cells Nude mice with subcutaneous ovarian tumor | Co-encapsulating CHQ with chemotherapeutic agents sensitized resistant cells to therapy, while prevented systemic toxicity. | [65] |
| Liposomes | n.a. | n.a. | PTX | 54-57 | Neutral | Carcinomas (lung/ovarian); Sarcoma | PTX-resistant human cells (lung carcinoma: A549/T; mouse sarcoma (S180), nude female mice bearing subcutaneous lung tumor or sarcoma | The study compared the efficacy of PTX-CHQ co-loaded liposomes with a mixture of liposomes individually loaded with PTX and CHQ, and free administered drugs. The co-delivery of both drugs showed more suitable pharmacokinetics, leading to more efficient tumor growth inhibition | [90] |
| Poly(ethyleneimine) dendrimers | n.a. | Triphenylphosphonium cations | n.a. | 60 | positive | Breast cancer | Human breast cancer cell lines (MCF-7, MDA-MB- 231, and SK-BR-3) | Overall, PTPP-CHQ caused mitochondrial superoxide formation (as a measure of mitochondria stress) to the adherent MCF-7 cells, whereas non-encapsulated CHQ did not induce significant alterations during that same time. | [92] |
| Poly(ethyleneimine) dendrimers | n.a. | Triphenylphosphonium cations | n.a. | 100 | Positive | Prostate cancer | DU145 human prostate cancer cells, PC3 cell lines; mice bearing tumor subcutaneous xenografts | The synthesized NPs could successfully encapsulate both DOX and CHQ. These NPs exhibit effective mitochondrial targeting and significantly improve the anticancer effectiveness of both drugs. The combination of Dox/CQH-loaded NPs leaded to a higher concentration of | [91] |

| | | | | | | | | | |
|---|---|---|---|---|---|---|---|---|---|
| | | | | | | | | CHQ into the tumor cells, enhancing the effect of the drug. | |
| PLGA NPs | PVA | n.a. | pDNA | 100-160 | Negative | Colon cancer | Human embryonic kidney (HEK293) and mouse colon carcinoma cell (CT26); male mice bearing colon cancer subcutaneous xenografts | The Ca-CHQ-pDNA-PLGA-NP was successfully constructed for gene delivery *in vivo*. Tt was demonstrated remarkable *in vivo* tumor targeting efficiency, prolonged circulation time, and enhanced tumor growth inhibition activity. The NPs were proved to be safe both *in vitro* and *in vivo*. | [93] |
| P(NIPAM-Aac) PNA nanogel | n.a. | n.a. | DOX | 200 | Negative | Breast cancer | Human breast cancer cell line with estrogen (MCF-7), mice bearing subcutaneous xenografts | The combination of loaded CHQ and DOX -loaded nanogels significantly inhibit cancer cell growth *in vivo*. | [94] |
| PLGA NPs | TPGS | n.a. | DOX | 174 | Negative | Breast Cancer | Human PTX resistant and (A549/Taxol) non-resistant lung cancer cells (A549) | NPDOX+CHQ dissociate in weakly acidic environment found in tumor cells, facilitating the release of the encapsulated drugs. | [95] |
| Chitosan NPs | n.a. | n.a. | Gefitinib | 81 | Positive | Liver carcinoma | Gefitinib-resistant (QGY/Gef) and non-resistant (QGY) hepatocellular carcinoma cells | CHQ and gefitinib co-loaded chitosan NPs overcome acquired resistance and improve cancer treatment efficacy by enhancing apoptosis and inhibiting cell autophagy. especially towards resistant strains. | [96] |
| Targeted Lipid NPs | PEG | RGD peptide | DHA | 195 | Negative | Colorectal cancer and Liver Metastasis | Human colorectal cancer cells (HCT116 and SW480), healthy human colon cells (NCM460), male nude mice with orthotopic metastasis of colorectal cancer | The developed formulation suppressed colorectal cancer proliferation and liver metastasis more efficiently than free combined therapy. DHA and CHQ increased ROS levels, causing cell death and promoting drug release. | [97] |
| ZIF-8 nanoplatform | Hyaluronic acid | n.a. | Polyoxometalates | 285 | Negative | Ovarian Cancer | Human ovarian cancer cells (SKOV3) | ZCPH nanoplatform remarkable photothermal therapy (PTT) potential, anti-inflammatory, and anti-autophagy capabilities. Co-encapsulation of POMs and CHQ into ZCPH leaded to the inhibition of the progression of the ovarian cancer. | [98] |

| | | | | | | | | | |
|---|---|---|---|---|---|---|---|---|---|
| Gold NPs | 11-mercaptoun decanoic acid | n.a. | n.a. | 7 | Negative | Breast Cancer | Human breast cancer cells (MCF-7) | CHQ - Gold NPs promoted drug's cytotoxicity in MCF-7 cells, with necrosis mediated by CHQ-induced autophagy being the primary mechanism of cell death. CHQ release was induced at lower PH. | [99, 145] |
| PLGA NPs | PVA | n.a. | n.a. | 205 | Negative | Pancreatic cancer | , Female mice with orthotopic pancreatic tumors of Pancreatic cancer cell line (SUIT-2), patient-derived PSCs | CQ-NPs pre-treatment enhanced gemcitabine's antitumor effect by reducing PSC activation in *vivo*, at lower concentration comparing to free drug. This suggests that the use of this nanocarrier could potentially decrease the required dosage of chloroquine and diminish its systemic toxicity. | [100] |
| Mesoporous silica NPs | PEG; PDMAEMA; PDEAEMA | n.a. | DNA and siRNA | 130/170 | Positive | Melanoma | B16F10 murine melanoma cells | CHQ co-loading in the NPs containing nucleic acids enhanced gene transfection and silencing activity compared to NPs without loaded CHQ. | [101] |

**Abbreviations**: Poly (methacrylic acid)(PMA); Poly (l-lactic acid)(PLA); Methoxy poly (ethylene glycol)(M-PEG); Doxorubicin (DOX); Paclitaxel (PTX); Triphenylphosphonium-functionalized hyperbranched polymer (PTPP); poly (ethyleneimine) (PEI); poly(lactic-co-glycolic acid) (PLGA); Biodegradable calcium phosphate (CaPi); N-Isopropylacrylamide (NIPAM); acrylic acid (AAc); alpha-tocopherol polyethylene glycol 1000 succinate (TPGS); Poly (ethylene glycol) PEG; Dihydroartemisinin (DHA); Hyaluronic acid (HA); Polyoxometalates(POM); ZIF-8/CHQ/POM/HA (ZCPH); Mesoporous Silica (MSN).

# A2. Calibration Curves

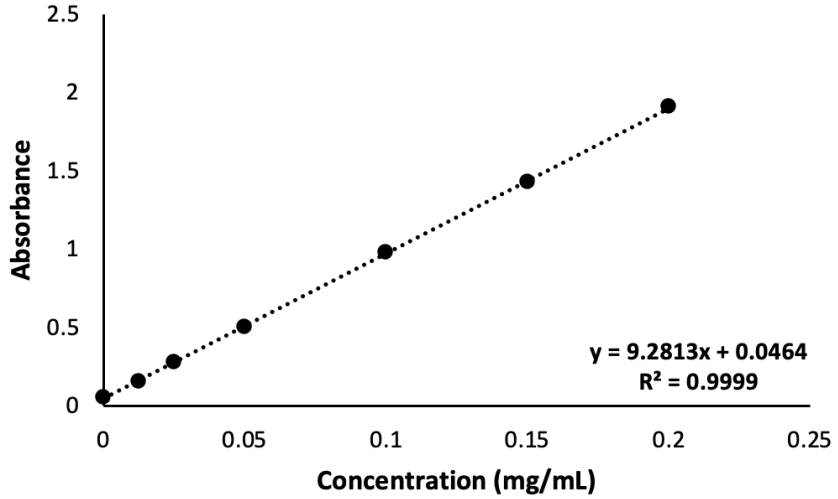


*Figure A2. 1: Absorbance calibration curve CHQ in PVA 1% to determine the EE.*

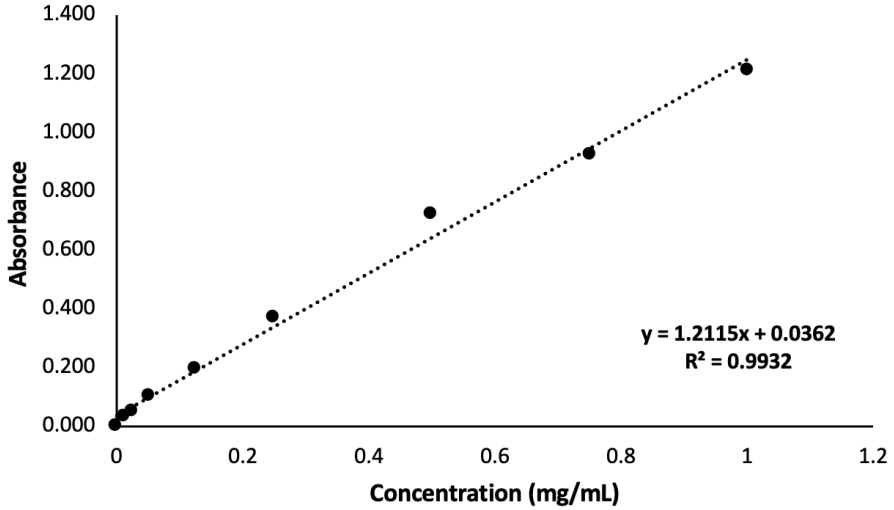


*Figure A2. 2:Absorbance calibration curve of Tf using the BCA kit for Tf quantification.*

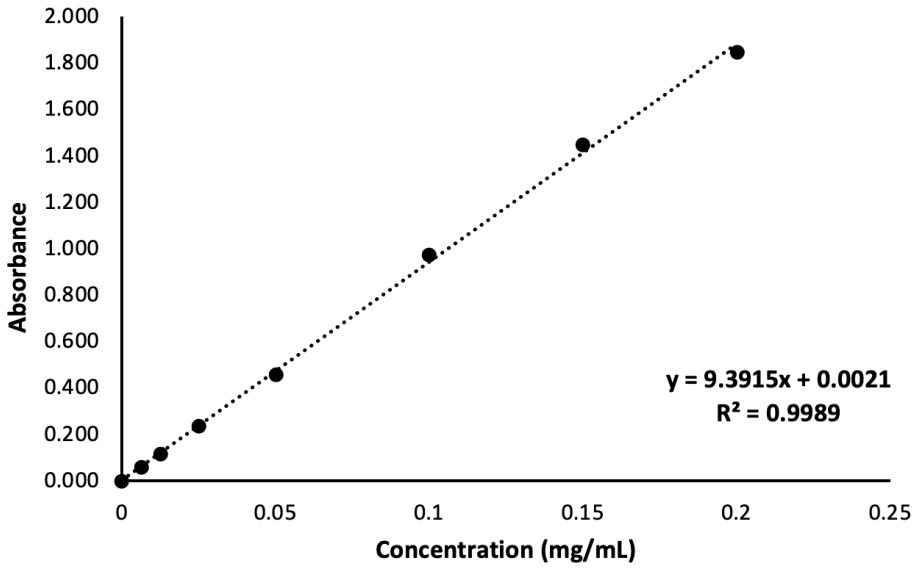


*Figure A2. 3: Absorbance calibration curve of CHQ in PBS (pH 7.4).*

# A3. Experimental Design

*Table A3. 1: Statistical Analysis of the responses using ANOVA.*

| **Parameter** | | | **Size** | | |
|---|---|---|---|---|---|
| | **SS** | **dF** | **MS** | **F-Value** | **p-Value** |
| **Model** | 96217.71 | 24 | 4009.07 | 140.16 | 0.0071 |
| **Residual** | | | | | |
| **Lack of Fit** | | | | | |
| **Pure Error** | 57.21 | 2 | 28.6 | | |
| **Cor Total** | 96274.92 | 26 | | | |
| **$R^2$** | | | 0.9994 | | |
| **Parameter** | | | **PDI** | | |
| | **SS** | **dF** | **MS** | **F-Value** | **p-Value** |
| **Model** | 0.1297 | 24 | 0.0054 | 94.27 | 0.0105 |
| **Residual** | | | | | |
| **Lack of Fit** | | | | | |
| **Pure Error** | 0.0001 | 2 | 0.0001 | | |
| **Cor Total** | 0.1298 | 26 | | | |
| **$R^2$** | | | 0.9991 | | |
| **Parameter** | | | **Zeta Potential** | | |
| | **SS** | **dF** | **MS** | **F-Value** | **p-Value** |
| **Model** | 282.58 | 24 | 11.77 | 36.42 | 0.0271 |
| **Residual** | | | | | |
| **Lack of Fit** | | | | | |
| **Pure Error** | 0.6467 | 2 | 0.3233 | | |
| **Cor Total** | 283.23 | 26 | | | |
| **$R^2$** | | | 0.9977 | | |
| **Parameter** | | | **EE** | | |
| | **SS** | **dF** | **MS** | **F-Value** | **p-Value** |
| **Model** | 11476.50 | 24 | 478.19 | 866.81 | 0.0012 |
| **Residual** | | | | | |
| **Lack of Fit** | | | | | |
| **Pure Error** | 1.10 | 2 | 0.5517 | | |
| **Cor Total** | 11477.60 | 26 | | | |
| **$R^2$** | | | 0.9999 | | |

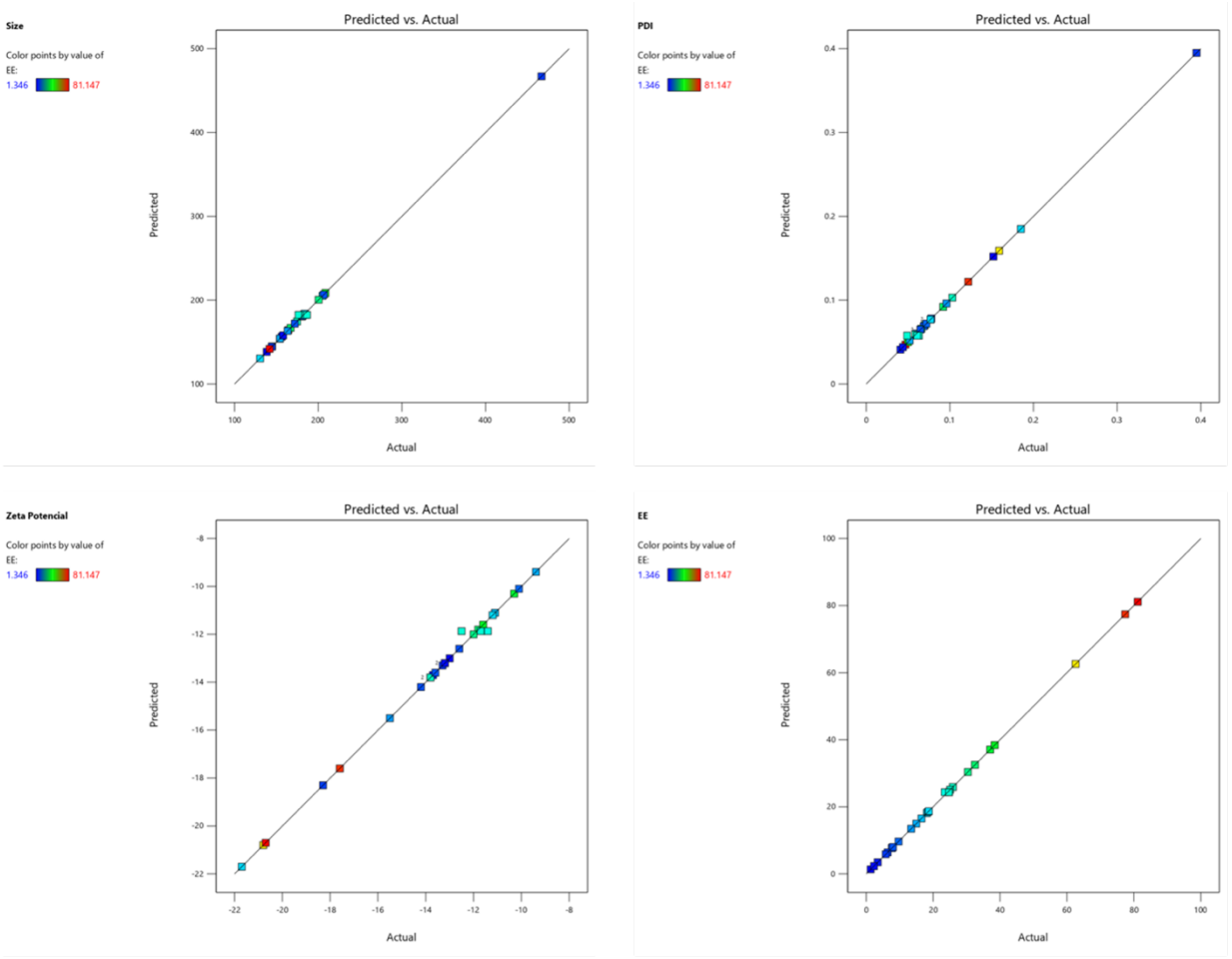


*Figure A3. 1: Correlation between the experimentally determined values and the predicted values for each significant variable.*

*Table A3. 2: ANOVA analysis applying a quartic model for size response.*

| Source | Sum of Squares | df | Mean Square | F-value | p-value | |
|---|---|---|---|---|---|---|
| **Model** | 96217.71 | 24 | 4009.07 | 140.16 | 0.0071 | significant |
| A-mPLGA | 1280.18 | 1 | 1280.18 | 44.76 | 0.0216 | |
| B-% Sonication | 158.42 | 1 | 158.42 | 5.54 | 0.1429 | |
| C-%PVA | 47740.5 | 1 | 47740.5 | 1669.05 | 0.0006 | |
| D-Water | 210.13 | 1 | 210.13 | 7.35 | 0.1134 | |
| AB | 39.38 | 1 | 39.38 | 1.38 | 0.3615 | |
| AC | 51.48 | 1 | 51.48 | 1.8 | 0.3118 | |
| AD | 144.6 | 1 | 144.6 | 5.06 | 0.1535 | |
| BC | 41.93 | 1 | 41.93 | 1.47 | 0.3497 | |
| BD | 2.81 | 1 | 2.81 | 0.0981 | 0.7838 | |
| CD | 286.46 | 1 | 286.46 | 10.01 | 0.087 | |
| $A^2$ | 859.75 | 1 | 859.75 | 30.06 | 0.0317 | |
| $B^2$ | 450.08 | 1 | 450.08 | 15.74 | 0.0581 | |
| $C^2$ | 20290.4 | 1 | 20290.4 | 709.37 | 0.0014 | |
| $D^2$ | 93.28 | 1 | 93.28 | 3.26 | 0.2127 | |
| ABC | 66.02 | 1 | 66.02 | 2.31 | 0.2681 | |
| ABD | 1.16 | 1 | 1.16 | 0.0404 | 0.8593 | |
| ACD | 42.58 | 1 | 42.58 | 1.49 | 0.3468 | |
| BCD | 19.14 | 1 | 19.14 | 0.6692 | 0.4993 | |
| $A^2B$ | 11.7 | 1 | 11.7 | 0.409 | 0.588 | |
| $A^2C$ | 28458.53 | 1 | 28458.53 | 994.94 | 0.001 | |
| $A^2D$ | 116.8 | 1 | 116.8 | 4.08 | 0.1807 | |
| $AB^2$ | 6.58 | 1 | 6.58 | 0.2299 | 0.6789 | |
| ABCD | 0.9506 | 1 | 0.9506 | 0.0332 | 0.8721 | |
| $A^2B^2$ | 2572.13 | 1 | 2572.13 | 89.92 | 0.0109 | |
| **Pure Error** | 57.21 | 2 | 28.6 | | | |
| **Cor Total** | 96274.92 | 26 | | | | |
| **$R^2$** | | | 0.9994 | | | |

*Table A3. 3: ANOVA analysis applying a quartic model for PDI response.*

| Source | Sum of Squares | df | Mean Square | F-value | p-value | |
|---|---|---|---|---|---|---|
| **Model** | 0.1297 | 24 | 0.0054 | 94.27 | 0.0105 | significant |
| A-mPLGA | 0.0064 | 1 | 0.0064 | 111.36 | 0.0089 | |
| B-% Sonication | 0.0001 | 1 | 0.0001 | 1.47 | 0.3486 | |
| C-%PVA | 0.0616 | 1 | 0.0616 | 1074.43 | 0.0009 | |
| D-Water | 0.0002 | 1 | 0.0002 | 3.15 | 0.218 | |
| AB | 0.0003 | 1 | 0.0003 | 5.04 | 0.1539 | |
| AC | 0.0003 | 1 | 0.0003 | 4.75 | 0.1612 | |
| AD | 0.0025 | 1 | 0.0025 | 42.74 | 0.0226 | |
| BC | 0.0005 | 1 | 0.0005 | 9.23 | 0.0934 | |
| BD | 0.0001 | 1 | 0.0001 | 1.12 | 0.4015 | |
| CD | 0.0028 | 1 | 0.0028 | 48.07 | 0.0202 | |
| $A^2$ | 0.006 | 1 | 0.006 | 105.01 | 0.0094 | |
| $B^2$ | 8.33E-07 | 1 | 8.33E-07 | 0.0145 | 0.9151 | |
| $C^2$ | 0.0314 | 1 | 0.0314 | 548.16 | 0.0018 | |
| $D^2$ | 0.001 | 1 | 0.001 | 17.4 | 0.0529 | |
| ABC | 9.00E-06 | 1 | 9.00E-06 | 0.157 | 0.7302 | |
| ABD | 0.0009 | 1 | 0.0009 | 15.7 | 0.0582 | |
| ACD | 0.0016 | 1 | 0.0016 | 28.61 | 0.0332 | |
| BCD | 0.0007 | 1 | 0.0007 | 11.79 | 0.0754 | |
| $A^2B$ | 3.84E-07 | 1 | 3.84E-07 | 0.0067 | 0.9423 | |
| $A^2C$ | 0.0498 | 1 | 0.0498 | 868.22 | 0.0011 | |
| $A^2D$ | 0.0002 | 1 | 0.0002 | 4.18 | 0.1775 | |
| $AB^2$ | 0.0016 | 1 | 0.0016 | 27.2 | 0.0349 | |
| ABCD | 0 | 1 | 0 | 0.6279 | 0.5112 | |
| $A^2B^2$ | 0.0128 | 1 | 0.0128 | 222.74 | 0.0045 | |
| **Pure Error** | 0.0001 | 2 | 0.0001 | | | |
| **Cor Total** | 0.1298 | 26 | | | | |
| **$R^2$** | | | 0.9991 | | | |

*Table A3. 4:ANOVA analysis applying a quartic model for ZP response.*

| Source | Sum of Squares | df | Mean Square | F-value | p-value | |
|---|---|---|---|---|---|---|
| **Model** | 282.58 | 24 | 11.77 | 36.42 | 0.0271 | significant |
| A-mPLGA | 67.28 | 1 | 67.28 | 208.08 | 0.0048 | |
| B-% Sonication | 8.86 | 1 | 8.86 | 27.41 | 0.0346 | |
| C-%PVA | 0.005 | 1 | 0.005 | 0.0155 | 0.9124 | |
| D-Water | 9.25 | 1 | 9.25 | 28.59 | 0.0332 | |
| AB | 0.1806 | 1 | 0.1806 | 0.5586 | 0.5327 | |
| AC | 5.18 | 1 | 5.18 | 16.01 | 0.0572 | |
| AD | 0.0306 | 1 | 0.0306 | 0.0947 | 0.7874 | |
| BC | 5.64 | 1 | 5.64 | 17.45 | 0.0528 | |
| BD | 0.2256 | 1 | 0.2256 | 0.6978 | 0.4914 | |
| CD | 1.38 | 1 | 1.38 | 4.27 | 0.1748 | |
| $A^2$ | 19.52 | 1 | 19.52 | 60.38 | 0.0162 | |
| $B^2$ | 0.1658 | 1 | 0.1658 | 0.5127 | 0.5483 | |
| $C^2$ | 2.3 | 1 | 2.3 | 7.1 | 0.1167 | |
| $D^2$ | 2.64 | 1 | 2.64 | 8.17 | 0.1037 | |
| ABC | 5.88 | 1 | 5.88 | 18.19 | 0.0508 | |
| ABD | 8.56 | 1 | 8.56 | 26.46 | 0.0358 | |
| ACD | 9.77 | 1 | 9.77 | 30.2 | 0.0316 | |
| BCD | 8.27 | 1 | 8.27 | 25.56 | 0.037 | |
| $A^2B$ | 6.68 | 1 | 6.68 | 20.66 | 0.0452 | |
| $A^2C$ | 4.17 | 1 | 4.17 | 12.9 | 0.0695 | |
| $A^2D$ | 10.24 | 1 | 10.24 | 31.68 | 0.0301 | |
| $AB^2$ | 11.04 | 1 | 11.04 | 34.15 | 0.0281 | |
| ABCD | 15.41 | 1 | 15.41 | 47.65 | 0.0203 | |
| $A^2B^2$ | 0.8057 | 1 | 0.8057 | 2.49 | 0.2552 | |
| **Pure Error** | 0.6467 | 2 | 0.3233 | | | |
| **Cor Total** | 283.23 | 26 | | | | |
| **$R^2$** | | | 0.9977 | | | |

*Table A3. 5:ANOVA analysis applying a quartic model for EE response.*

| Source | Sum of Squares | df | Mean Square | F-value | p-value | |
|---|---|---|---|---|---|---|
| **Model** | 11476.5 | 24 | 478.19 | 866.81 | 0.0012 | significant |
| A-mPLGA | 39.09 | 1 | 39.09 | 70.86 | 0.0138 | |
| B-% Sonication | 24.44 | 1 | 24.44 | 44.3 | 0.0218 | |
| C-%PVA | 6.19 | 1 | 6.19 | 11.22 | 0.0787 | |
| D-Water | 13.86 | 1 | 13.86 | 25.12 | 0.0376 | |
| AB | 291.05 | 1 | 291.05 | 527.59 | 0.0019 | |
| AC | 13.44 | 1 | 13.44 | 24.36 | 0.0387 | |
| AD | 159.52 | 1 | 159.52 | 289.17 | 0.0034 | |
| BC | 128.52 | 1 | 128.52 | 232.97 | 0.0043 | |
| BD | 1295.44 | 1 | 1295.44 | 2348.24 | 0.0004 | |
| CD | 1033.22 | 1 | 1033.22 | 1872.91 | 0.0005 | |
| $A^2$ | 126.62 | 1 | 126.62 | 229.53 | 0.0043 | |
| $B^2$ | 198.3 | 1 | 198.3 | 359.45 | 0.0028 | |
| $C^2$ | 492.7 | 1 | 492.7 | 893.11 | 0.0011 | |
| $D^2$ | 82.33 | 1 | 82.33 | 149.23 | 0.0066 | |
| ABC | 6.03 | 1 | 6.03 | 10.94 | 0.0805 | |
| ABD | 45.71 | 1 | 45.71 | 82.87 | 0.0119 | |
| ACD | 113.77 | 1 | 113.77 | 206.23 | 0.0048 | |
| BCD | 2828.51 | 1 | 2828.51 | 5127.22 | 0.0002 | |
| $A^2B$ | 0.0215 | 1 | 0.0215 | 0.039 | 0.8617 | |
| $A^2C$ | 31.2 | 1 | 31.2 | 56.56 | 0.0172 | |
| $A^2D$ | 39.2 | 1 | 39.2 | 71.05 | 0.0138 | |
| $AB^2$ | 19.36 | 1 | 19.36 | 35.1 | 0.0273 | |
| ABCD | 2868.81 | 1 | 2868.81 | 5200.27 | 0.0002 | |
| $A^2B^2$ | 1071.02 | 1 | 1071.02 | 1941.42 | 0.0005 | |
| **Pure Error** | 1.1 | 2 | 0.5517 | | | |
| **Cor Total** | 11477.6 | 26 | | | | |
| **$R^2$** | | | 0.9999 | | | |

*Table A3. 6:ANOVA analysis applying a quartic model for Yield response.*

| Source | Sum of Squares | df | Mean Square | F-value | p-value | |
|---|---|---|---|---|---|---|
| **Model** | 1688.51 | 24 | 70.35 | 13.93 | 0.0691 | not significant |
| A-mPLGA | 3.62 | 1 | 3.62 | 0.7166 | 0.4864 | |
| B-% Sonication | 25.7 | 1 | 25.7 | 5.09 | 0.1527 | |
| C-%PVA | 79.88 | 1 | 79.88 | 15.82 | 0.0578 | |
| D-Water | 48.31 | 1 | 48.31 | 9.57 | 0.0905 | |
| AB | 3.53 | 1 | 3.53 | 0.6982 | 0.4913 | |
| AC | 93.94 | 1 | 93.94 | 18.61 | 0.0498 | |
| AD | 5.77 | 1 | 5.77 | 1.14 | 0.3969 | |
| BC | 2.26 | 1 | 2.26 | 0.4471 | 0.5725 | |
| BD | 10.84 | 1 | 10.84 | 2.15 | 0.2805 | |
| CD | 31.22 | 1 | 31.22 | 6.18 | 0.1307 | |
| $A^2$ | 368.27 | 1 | 368.27 | 72.94 | 0.0134 | |
| $B^2$ | 46.7 | 1 | 46.7 | 9.25 | 0.0932 | |
| $C^2$ | 317.01 | 1 | 317.01 | 62.79 | 0.0156 | |
| $D^2$ | 101.09 | 1 | 101.09 | 20.02 | 0.0465 | |
| ABC | 5.19 | 1 | 5.19 | 1.03 | 0.4175 | |
| ABD | 44.46 | 1 | 44.46 | 8.8 | 0.0973 | |
| ACD | 39.78 | 1 | 39.78 | 7.88 | 0.1069 | |
| BCD | 2.71 | 1 | 2.71 | 0.5376 | 0.5397 | |
| $A^2B$ | 0.8715 | 1 | 0.8715 | 0.1726 | 0.7181 | |
| $A^2C$ | 196.17 | 1 | 196.17 | 38.85 | 0.0248 | |
| $A^2D$ | 25.76 | 1 | 25.76 | 5.1 | 0.1524 | |
| $AB^2$ | 19.75 | 1 | 19.75 | 3.91 | 0.1866 | |
| ABCD | 492.73 | 1 | 492.73 | 97.59 | 0.0101 | |
| $A^2B^2$ | 266.38 | 1 | 266.38 | 52.76 | 0.0184 | |
| **Pure Error** | 10.1 | 2 | 5.05 | | | |
| **Cor Total** | 1698.61 | 26 | | | | |
| **$R^2$** | | | 0.9941 | | | |

**A3.7 - Regression Equation Size:**

**Size** = 182.47 + 17.89 A –109.25 C -13.38 $A^2$ + 65.02 $C^2$+ 94.3 $A^2C$– 48 $A^2B^2$

**Legend:** PLGA mass (A), %Sonication (B) and %PVA (C)

**A3.8 - Regression Equation PDI:**

**PDI** = 0.0577 – 0.04 A– 0.1241 C+ 0.0124 AD– 0.0131 CD + 0.0354 $A^2$ + 0.0809 $C^2$ + 0.0101 ACD + 0.1247 $A^2C$ + 0.0221 $AB^2$– 0.107 $A^2B^2$

**Legend:** PLGA mass (A), %Sonication (B), %PVA (C) and Water Volume (D)

**A3.9 - Regression Equation ZP:**

**ZP** = -11.87 + 4.1 A + 1.49 B + 1.52 D – 2.02 $A^2$ + 0.7312 ABD + 0.7812 ACD – 0.7188 BCD – 1.44 $A^2B$– 1.79 $A^2D$ – 1.86 $AB^2$ + 0.9813 ABCD

**Legend:** PLGA mass (A), %Sonication (B), %PVA (C) and Water Volume (D)

**A3.10 - Regression Equation EE:**

**EE** = 24.36 – 3.13 A + 2.47 B + 1.86 D – 4.27 AB – 0.9164 AC + 3.16 AD – 2.83 BC + 9 BD + 8.04 CD – 5.14 $A^2$ – 6.43 $B^2$ – 10.13 $C^2$ – 4.14 $D^2$ + 1.69 ABD – 2.67 ACD + 13.3 BCD + 3.12 $A^2C$ – 3.5 $A^2D$ – 2.46 $AB^2$ – 13.39 ABCD + 30.98 $A^2B^2$

**Legend:** PLGA mass (A), %Sonication (B), %PVA (C) and Water Volume (D)